Geomagnetic polarity and carbon isotopic stratigraphic assessment of the late Carnian -earliest Norian in Svalbard: evidence for a major hiatus and improved Boreal to Tethyan correlation

Mark W. Hounslow[1,2], Samuel E. Harris[3], Vassil Karloukovski[1] & Atle Mørk[4]

[1]Lancaster Environment Centre, Lancaster University, Lancaster, UK.

[2]Earth, Ocean and Ecological Sciences, Univ. of Liverpool, Jane Herdman Building, Liverpool, UK.

[3]School of Archaeological and Forensic Sciences, University of Bradford, Bradford, BD7 1DP, UK.

[4] Atle Arctic, Trondheim, Norway.

E-mail of corresponding author (Mark W. Hounslow): mark.w.hounslow@gmail.com

Combining magnetostratigraphy and organic carbon isotopic changes has allowed a more precise position to be determined for the base of the Norian in Svalbard successions. A magnetostratigraphy is constructed from two sections (Binnedalen, Nørdstefjellet) from the northern end of Hopen Island (southern Svalbard archipelago), from the De Geerdalen Formation and the lowest part of the Flatsalen Formation. A magnetostratigraphy is also determined from the upper part of the De Geerdalen Formation on Wilhelmøya (eastern Svalbard). On Hopen a composite magnetostratigraphy tied to the Binnedalen section was constructed using correlation based on detailed photographs and logs of the adjacent cliffs. The palaeomagnetic data shows a strong Brunhes overprint, but mean palaeomagnetic directions pass the reversal test and are consistent with other Triassic virtual geomagnetic palaeopole data from Svalbard. The palaeomagnetic signal is carried by magnetite. Organic carbon isotope data identifies three negative excursions in the Hopen succession— below the Hopen Member, within the upper Hopen Member and at the De Geerdalen – Flatsalen formation boundary. The carbon isotope variations are correlated to Tuvalian (late Carnian) excursions seen in lower paleolatitude sections. The magnetostratigraphy of the Isfjorden Member from Wilhelmøya and central Spitsbergen are similar, and when integrated with the carbon isotope stratigraphy suggests that the Isfjorden Member is not equivalent to the units of the De Geerdalen Formation exposed on northern Hopen, but is older. These relationships suggest the sequence boundary at the base of the Wilhelmøya Subgroup probably cuts down into mid Tuvalian age strata of the De Geerdalen Formation in Spitsbergen and Wilhelmøya, but only into the latest Tuvalian strata on Hopen. A revised Tuvalian geomagnetic polarity scale is also proposed, linked to the carbon isotope excursions.

Keywords: Carnian-Norian boundary, magnetostratigraphy, organic carbon isotope, De Geerdalen Formation, Hopen Member

Received 10. May 2021/Accepted 30. Decembre 2021/ Published online xxx

Hounslow, M.W. Harris, S.E, Karloukovski, V. & Mørk, A. 2022: Geomagnetic polarity and carbon isotopic stratigraphic assessment of the late Carnian -earliest Norian in Svalbard: evidence for a major hiatus and improved Boreal to Tethyan correlation. *Norwegian Journal*

of Geology MISSING PLANNED ISSUE AND ARCITCLE NUMBER AND DOI.

Introduction

The Upper Triassic in the Barents Sea and Svalbard consists of the Kapp Toscana Group which is divided into two subgroups (Figs. 1 & 2a). These subgroups show major regional differences in sedimentary systems (Riis et al., 2008; Klausen et al., 2015), an upwards decrease in accumulation rates (Anell et al., 2014; Rismyhr et al., 2018) and an increase in sandstone maturity (Mørk, 1999). This major boundary is marked by the base of the Wilhelmøya Subgroup (Flatsalen and Knorringfjellet formations) in Svalbard and the base of the Fruholmen Formation in the Barents Sea (Fig. 2a).

The inferred position of the Carnian–Norian boundary with respect to the lithostratigraphy and sequence stratigraphy has varied between studies, in part due to the poor chronostratigraphic constraints available from the underlying De Geerdalen Formation. The Carnian–Norian boundary has been variably placed: 1) in the mid De Geerdalen Formation (Hochuli et al., 1989; Harland, 1997), 2) at the base of the Isfjorden Member of the De Geerdalen Formation (Pčelina, 1972; Riis et al., 2008; Nagy et al., 2011; Anell et al., 2014; Mueller et al., 2016; Paterson et al., 2016; Lord et al., 2019; Fig. 2a); 3) in the top-most De Geerdalen or Snadd formations (Glørstad-Clark et al., 2010; Klausen et al., 2015; Paterson & Mangerud, 2015; Gilmullina et al., 2021), and 4) at the base of the Wilhelmøya Subgroup (Lord et al., 2014; Vigran et al., 2014; Paterson & Mangerud, 2020, Gilmullina et al., 2021).

Part of the uncertainty in the placement of the base of the Norian in these units relates to the lack of an agreed global stratotype section and point (GSSP) for the base of the Norian; something that has been resolved recently (Hounslow et al., 2021b), but the GSSP remains to be ratified by the International Commission on Stratigraphy. The base Norian is now expected to be placed at the first occurrence of the flat clam *Halobia austriaca* in the Pizzo Mondello section in Sicily (Hounslow et al., 2021b).

In addition, age control using the multiple sets of palynological zonations proposed (Fig. 2b), can only be generated through their relationship to other chronostratigraphic correlation tools, since the ranges of many palynomorphs in the Svalbard and Barents Sea region generally extend into older intervals than successions from more southerly palaeolatitudes (such as in the Germanic Basin), due to climatic and environmental controls (Smith, 1982; Cirili, 2010, Paterson & Mangerud, 2020). The key tools for providing the independent chronostratigraphic correlation are therefore the sporadic ammonoid occurrences (Smith, 1982; Korchinskaya, 1980; Dagys & Weitschat 1993, Fig. 2a), and magnetostratigraphy (Hounslow et al., 2007; Lord et al., 2014).

Magnetostratigraphy provides age control through correlating the pattern of polarity changes between sections. Polarity boundaries are ideally synchronous (at a few ka uncertainty) at a global scale, providing a means for detailed chronostratigraphic correlation. The age-calibrated pattern of polarity changes in the Late Triassic is reasonably well known (Krystyn

et al., 2002; Gallet et al., 2003; Hounslow & Muttoni, 2010; Maron et al., 2019), although the pattern of polarity changes in the mid Carnian is less clear. The magnetostratigraphy of the early Carnian (Julian Substage) is reasonably well known from Tethyan sections at Prati di Stuores (Broglio Loriga et al., 1999; Mietto et al., 2012), Bolücektasi Tepe (Gallet et al., 1992) and Mayerling (Gallet et al., 1994, 1998). The magnetostratigraphy of the late Carnian (Tuvalian Substage) and early Norian (Lacian Substage) is well studied from sections at Pizzo Mondello (Muttoni et al., 2004), Silická Brezová (Channell et al., 2003) and Kavaalani (Gallet et al., 2000) and some other sections (Maron et al., 2017). The geomagnetic polarity during the mid Carnian is either inferred as unknown (Maron et al., 2019), or the magnetostratigraphy from the poorly dated Stockton Formation of the Newark Supergroup is projected downwards into this interval (Hounslow & Muttoni, 2010; Kent et al., 2017; Zhang et al., 2020).

The aims of this work have been to provide a magnetostratigraphy from the Kapp Toscana Group on Hopen and Wilhelmøya (Fig. 1), in sections which cover the interval from the upper parts of the De Geerdalen Formation into the lower part of the Flatsalen Formation (Fig. 2a), thereby addressing the issue of a more precise position for the base of the Norian. We also use organic carbon isotope stratigraphy to constrain polarity correlations in this interval, by proposing a succession of negative carbon isotope excursions in the Tuvalian and earliest Lacian that allow additional correlation to low palaeolatitude sections. This analysis also provides a revised geomagnetic polarity record through the Tuvalian tied to the carbon isotope excursions.

Regional lithostratigraphy and sequence stratigraphy

The De Geerdalen Formation below the Isfjorden and Hopen members (Fig. 2a) consists of repeated coarsening-upward sandstone bodies separated by shales (Lord et al., 2017), inferred as prograding units. The sandstone bodies vary in thickness from a few metres up to 30 m and represent development of deltaic channel sandstones, coastal and shoreface sandstones and offshore sandstone bodies (Mørk et al*.,* 1982, Riis et al., 2008). The major sandstone bodies can show great thickness variations laterally, over several hundred metres, because of the development of channel systems. The De Geerdalen Formation thickens from 200 – 300 m on central and eastern Spitsbergen (Mørk et al., 1999; Mørk & Worsley, 2006) to about 700 m at Hopen (Riis et al., 2008).

The Isfjorden Member (50 – 70 m thick) is dominated by siltstone and shale with thin sandstone beds, occasionally phosphatic and most significantly bioclastic beds and red to green nodular (i.e., in part calcrete) palaeosols (not seen in the underlying parts of the De Geerdalen Formation; Haugen, 2016; Lord et al., 2017). The Hopen Member. (66 –70 m thick) is a heterolithic unit without coals or palaeosols, comprising dark shales and interbedded hummocky cross-bedded sandstones, with rare bivalves (Lord et al., 2014). The N1 3rd order sequence of Klausen et al. (2015) is represented by the upper parts of the Hopen Member, with the lower parts of the Hopen Member and underlying De Geerdalen Formation (on Hopen) equivalent to the upper parts of the older C4 3rd order sequence (Fig. 2a).

On Spitsbergen and Wilhelmøya the Slottet Bed overlies the Isfjorden Member (Lord et al., 2017), but on Hopen it overlies the Hopen Member (Lord et al., 2014; Fig 2a). The Slottet Bed marks the base of the Wilhelmøya Subgroup over a large part of Svalbard. The Slottet Bed (often 2–3 m thick) is a regionally quite variable unit, in places a calcareous glauconitic sandstone with phosphatic nodules ranging to a calcareous siltstone and sometimes a polymict conglomerate. It is not known on Barentsøya and Edgeøya (Fig. 2a). Internal

channelling and planar and hummocky cross stratification are common in the sandier expressions of the Slottet Bed (Mørk et al., 1999; Lord et al., 2017; Rismyhr et al., 2018). In central and western Spitsbergen, the base of the Slottet Bed (lowest part of the Knorringfjellet Formation) is a combined subaerial unconformity which down-cuts into the underlying De Geerdalen Formation (Rismyhr et al., 2018). The Slottet Bed is likely a condensed transgressive deposit at the base of the Wilhelmøya Subgroup and represents the upper part of the N1 3rd order sequence of Klausen et al. (2015). On Hopen the overlying Flatsalen Formation (Wilhelmøya Subgroup) is a marine dark-grey shale unit with regularly spaced beds of bioturbated fine-grained sandstone, containing siderite-nodules (Lord et al., 2019). This represents the N2 and overlying R1 3rd order sequences of Klausen et al. (2015).

Biostratigraphy

On Svalbard, Carnian to Norian ammonoid dated units are restricted to two intervals. Firstly, in the lowest part of the Tschermakfjellet Formation where ammonoids define the *Stolleyites tenuis* Zone (Dagys & Weitschat 1993; Konstantinov, 2014; Fig. 2a), which immediately follows the earliest Carnian *Daxatina canadensis* Zone (Mietto et al., 2012), which is only found on Bjørnøya in the Skuld Formation (lithologically like the Tschermakfjellet Formation; Mørk et al., 1990; 1999).

Secondly, ammonoids from the mid and upper parts of the Flatsalen Formation on Hopen (Fig. 2a), described from studies of Russian workers (Konstantinov & Sobolev, 2000). From Hopen, Korčinskaya (1980) describes *Norosirenites nelgehensis*, *N. obruchevi* and "sirenites" *nabeshi* from the Flatsalen Formation, which in NE Asia occurs in the *Pinacoceras verchojanicum* Zone (Zakharov 1997; Konstantinov & Sobolev, 2000). Konstantinov & Klets (2009) and Bragin et al. (2012) correlate this zone to the mid parts of the early Norian. The Flatsalen Formation also contains nautoloids suggesting a similar relationship to the NE Asian Norian zonations (Konstantinov & Sobolev, 2000). In NE Asia the occurrence of the conodont *Norigondolella navicula* in the same beds bearing the P. *verchojanicum* Zone ammonoid fauna (Konstantinov et al., 2003; Bragin et al. 2012), suggests much the same correlation, with the range of *N. navicula* corresponding to the interval approximately from near the base of the Lacian-1 (Tethyan Jandianus Zone) to mid parts of Lacian-2 interval (Tethyan, Paulckei Zone), of Krystyn's (1980) Tethyan substage divisions (Krystyn et al., 2002; Orchard, 2010). The inferred base of the Norian expressed in the chronostratigraphy of the NE Asian ammonoid zonations is a level approximately at or slightly below the first occurrence of *H. austriaca* (i.e., base Norian GSSP) at the Pizzo Mondello section (Hounslow et al., 2021b).

The age equivalence of the Hopen and Isfjorden members has been proposed (Mørk et al., 2013; Lord et al., 2014), partly based on the marine intercalations throughout the Isfjorden Member. Whilst palynological zonations of the upper De Geerdalen Formation are well established on Hopen and in equivalent units in the Barents Sea (Fig. 2b), the palynological characterisation of the Isfjorden Member is less well defined. Palynological data for the Isfjorden Member come from the Festningen section in western Spitsbergen, and at Dalsnuten and the DH4-CO_2 core from central Spitsbergen (Vigran et al., 2014; Rismyhr et al., 2018). The upper part of the Isfjorden Member (in the DH4 core and Festningen section) has miospores indicating the *Protodiploxypinus* spp. Zone of Paterson & Mangerud (2020). The *Protodiploxypinus* spp. Zone also occurs in the Hopen Member (Fig. 2b), and locally in the upper c. 20 m of the underlying De Geerdalen Formation (Paterson & Mangerud, 2015), suggesting the Hopen and Isfjorden members may be partly correlative, or represent similar sets of palynofacies. However, from Dalsnuten the lower part of the Isfjorden Member contains common to dominant *Leschikisporis aduncus* (Vigran et al., 2014), the major

component of the underlying *L. aduncus* Zone (Paterson & Mangerud, 2020) of the De Geerdalen Formation, that underlies the Hopen Member on Hopen. This indicates a potentially older age for part of the Isfjorden Member in central Spitsbergen.

Sampling and intersection correlation

Oriented paleomagnetic samples were collected from two sections on the northern end of Hopen: A) The Binnedalen section during 2011 (Figs. 1c & 3), and B) a section on the NW cliff of Nørdstefjellet during 2010 (Figs. 1c & 4). The Binnedalen section has been extensively sampled for palynology (Paterson & Mangerud, 2015) and both sections have been studied for sedimentology (Lord et al., 2014). The Hopen outcrops represent only the upper part of the De Geerdalen Formation (Fig. 2a).

Paleomagnetic samples were also collected from the Tumlingodden section on Wilhelmøya above the dolerite sill in the section, covering a c. 100 m interval through the uppermost part of the De Geerdalen Formation and lowermost part (basal unit of Worsley, 1973) of the Flatsalen Formation (Figs. 1a & 5, SI Fig. S2). Haile et al. (2019) has described the lower part of the De Geerdalen Formation below the dolerite sill in the section. At Tumlingodden sampling started some 59 m stratigraphically above the dolerite intrusion that occurs in the middle parts of the De Geerdalen Formation, well above the apparent effects of heating from the underlying sill. A further 3 sample levels from the dolerite intrusion and its contact metamorphic interval were collected to investigate potential thermal overprint magnetisations on the palaeomagnetic data from the De Geerdalen Formation.

In each case samples were oriented with a magnetic compass and an orientation staff. Collected samples were re-oriented in plaster and cut into palaeomagnetic specimen cubes on a diamond saw (fragmented samples were glued together using Na-silicate or PVA glue). In most cases, several sister specimens were cut from each block to measure. A variety of lithologies were sampled including sandstones, siltstones and claystones.

The sampling levels from the Nørdstefjellet section on Hopen were correlated to the Binnedalen section, using field notes, and photo correlation of selected levels between the two sections (Figs. 3 & 4 and SI Fig. S1). Interpretation of the section photos allowed us to determine several bed-levels which could be correlated between the sections and mapped onto the logs of the sections. This allowed us to approximate the position of the Nørdstefjellet section samples onto the Binnedalen log, with an accuracy of about 1–2 metres (Fig. 6).

The inter-section correlations were controlled by 4 primary bed-levels:

1) **S1 level,** corresponding to the upper level of Solvi (2013) Channel-1 sandstone, which is clearly seen to pinch out to the North adjacent to the sampled Nørdstefjellet section (rightside of Fig. 4). This same bed-level is probably displaced by the fault to the north of the main Binnedalen section (rightside of Fig. 3) and constitutes the lowest part of the sampled section at Binnedalen.

2) **S2 level,** corresponding to the upper beds of the Channel-2 of Solvi (2013). This level can be traced from the cliffs to the south to intersect with the Nørdstefjellet section (Figs. 3 & 4 SI Fig. S1), and is clearly seen in the main Binnedalen section log as the dominant channel sandstone at around 55 m height (Fig. 3; sandstone channel off to the south of the photograph).

3) A distinctive thick shale layer (called **HMS**) in the upper part of the Hopen Member (Solvi, 2013; Lord et al., 2014) seen in the cliff photos of both sections (Figs. 3 & 4). This lies directly below a cliff-forming unit in the upper part of the Hopen Member. South of the Binnedalen section this shale layer becomes less distinct in the cliff photographs.

4) The Slottet Bed (**SL level;** Figs. 3 & 4) at the base of the Flatsalen Formation.

Within these basic divisions, secondary correlation levels were used:

A. The upper boundary of a strongly banded interval (many ~1 m-thick sandstone beds in shale) in the lower part of the sections (Figs. 3 & 4)

B. A prominent ledge about 5 m above the S2 level (Figs. 3 & 4). This bed-level correlation implies there are some substantial thickness variations in the beds which underlie and overlie this level.

HM1 to HM3, three distinctive intervals within the lower part of the Hopen Member, which can be correlated between these two sections (Figs. 3 & 4)

The detailed correlation of the sample heights from the Nørdstefjellet onto the Binnedalen section, using the bed-levels outlined above is indicated by the correlation lines in Fig. 6.

Methods

Palaeomagnetic methods

Measurements of natural remanent magnetisation (NRM) were made using a CCL cryogenic magnetometer (noise level ~2 μA/m), using three specimen positions (12 measurements of x,y,z in total), from which the magnetisation variance was determined. Other than when being measured or demagnetised, specimens were housed in Mu-metal boxes with an ambient magnetic field <10 nT. Low frequency magnetic susceptibility (K) was monitored after heating steps, measured using a Bartington Ltd. MS2B sensor to assess thermal alteration. The NRM of specimens from all sections were treated with a combination of thermal and alternating field (AF) demagnetisation. Thermal demagnetisation used a Magnetic Measurements Ltd. MMTD, and AF demagnetisation used a reverse-tumbling Molspin Ltd. demagnetiser. The magnetisation directions were extracted from the demagnetisation data using principal component analysis as implemented in the LINEFIND software (Kent et al., 1983). This analysis extracts characteristic magnetisation components (ChRM), utilising the variance from the multiple measurements at each demagnetisation step. The software has statistical procedures for objective identification of linear and planar structure. Details on using this program and its merits over conventional methods are in Hounslow et al. (2021a).

Specimen behaviour during demagnetisation was classified into two types. Firstly, S-type behaviour in which the ChRM could be defined, using three or more points on a straight-line segment, commonly directed through the origin. Specimens were visually classified into three sub-groups (S1, S2 and S3), with S1 having the least noisy line fits and most datapoints in the ChRM range and S3 the noisiest (S3 line fits had > = 3 datapoints). Secondly, T-type behaviour in which specimen data exhibited a great-circle path towards an interpreted Triassic-like direction. Specimens with T-type behaviour were classified qualitatively into best quality (T1) and inferior quality (T2, T3) great-circle trends, based on the directional scatter. Average fitting statistics for these qualitative demagnetisation classes are in SI Table S2.

Based on the specimen demagnetisation data, each specimen was assigned a qualitative polarity-quality rating. This comprised 7 classes, 3 for each of normal and reverse polarity, with the samples labelled N (or R) showing the best quality data, and N?, N?? (or R?, R??) for poorer quality data (Fig. 7). The last '?' class is for specimen data in which it is not possible to unambiguously interpret the geomagnetic polarity recorded. The virtual geomagnetic pole (VGP) latitude (Opdyke & Channell, 1996) of specimen data was

determined using the mean direction determined from the section as the reference pole (Pmagtool v.5 software was used; Hounslow, 2006). For the T-class specimens, the VGP latitudes were determined by using the point on the specimen great-circle plane nearest the appropriate section mean direction (i.e., 'all' means from Table 1; like in Hounslow et al., 2007; 2008a). We also use the VGP-mean dispersion (A95; Table 1) and the $A95_{min}$ and $A95_{max}$ thresholds of Deenen et al. (2011) as an expression of likely capture of secular variation in the directional data.

Carbon isotopes

A sub-sample from the palaeomagnetic samples was measured for $\delta^{13}C_{org}$. The ~20 g sub-sample was powdered in a ball mill, and carbonate minerals were removed by reacting the homogenised material with 6N HCl at 25°C for 24 hours, which also removes siderite and ankerite (Larson et al., 2008; Brodie et al., 2011). After reaction-ceased, residues were washed several times with distilled water to remove any traces of acids. Residues were then oven-dried at 50°C for 24 hours and subsequently re-powdered prior to $\delta^{13}C_{org}$ isotope analysis. Decarbonated residues were weighed into tin capsules and loaded into an auto-sampler connected to an Elementar Vario MICROcube, from where they were dropped into the furnace at 950ºC. Produced gases were passed (under He) through chemical traps to remove sulphur, excess oxygen, and water. Large sample volumes could be used, so we could reliably measure $\delta^{13}C_{org}$ down to around 0.02% total organic carbon. Percent total carbon (%C) and total nitrogen ($\%N_T$) were measured with a precision of c. 0.01%. Nitrogen was separated from CO_2 by temperature programmed desorption. The isotopic composition of the resultant purified CO_2 was then measured using an Isoprime100 Isotope mass spectrometer. Carbon isotope ratios are reported as delta values ($\delta^{13}C$) in per mil relative to the international VPDB scale (standards used: NBS-18 = -5.014‰; LSVEC = -46.6‰). Analytical precision (1σ) is estimated to be c. ± 0.15‰ for $\delta^{13}C_{org}$ based on the replicate analysis of pure, well-mixed, organic compounds used as laboratory calibration materials.

Results

For most lithologies the last useful thermal demagnetisation heating step was dictated by the onset of mineralogical alteration (i.e., start of the 'susceptibility crisis'), which for many specimens began at about 200–250ºC. This prevented much useful data thermal demagnetisation data beyond ~250ºC. Magnetic susceptibility measurements were made after each heating step to identify this susceptibility crisis step during initial runs. Following trials, identifying the crisis point with respect to lithology, specimens were subsequently AF demagnetised following thermal demagnetisation at temperatures just prior to the on-set of the susceptibility crisis. Tumbling AF demagnetisation was in 5 – 10 mT steps until magnetic fields of 70 – 90 mT. Thermal demagnetisation of isothermal remanent magnetisation (IRM) and IRM backfield demagnetisation indicates magnetite dominates the magnetic mineralogy (SI Figs. S6 & S7; SI Table S1).

A low-stability component (LT component) was typically isolated with thermal demagnetisation, with most LT components starting from 100 – 160ºC, until the early or occasionally mid stages of alternating field (AF) demagnetisation (see SI excel file for details). The LT directions show mean directions scattered around a northerly down-directed magnetisation with a mean inclination of ~83º (SI Fig. S3a). The expected inclinations (Inc.) for the Brunhes-age (i.e., 0.7 Ma to 0 Ma) magnetic field at the latitude of Hopen and Wilhelmøya are 83.3º and 84.6º , respectively. The mean LT component is similar in inclination in both Hopen sections and was probably acquired during the Brunhes.

For the Tumlingodden section the magnetisation in the dolerite sill (SI Fig. S3b) has a ChRM mean direction of Dec. = 191°, Inc. = -70° (α_{95} = 17.6°, k = 22.6, n = 5). The specimens from the De Geerdalen Formation in the section, mostly show typical LT component behaviour like samples on Hopen, without low-stability reverse polarity directions, as might be expected if heating or alteration had taken place due to the dolerite intrusion. Therefore, the demagnetisation data indicate the dolerite intrusion has not imparted the ChRM directions observed in the De Geerdalen Formation.

The ChRM was commonly defined starting with the last thermal demagnetisation steps (240–300°C), or the early stages of AF demagnetisation (Figs. 7 & 8). The end range of the ChRM component typically went to the 60 – 75 mT steps or the origin of the Zijderveld plot. In some specimens, noise imparted by the AF demagnetiser at high fields (>~75mT), often precluded origin-fits. S-type behaviour is seen in 38% and 20% of specimens from Hopen and Wilhelmøya, respectively. On Hopen only 2% of these S-type specimens are inferred to be reverse polarity (Fig. 9b, c), whereas on Wilhelmøya 50% are reverse polarity (Fig. 10b, c). Some 62% of specimens on both Hopen and Wilhelmøya displayed T-type behaviour (Figs. 9 & 10). On Hopen, these are dominated by specimens inferred to have reverse polarity Triassic magnetisations. This kind of polarity-related demagnetisation behaviour is common in Triassic and Permian samples from Svalbard (Hounslow et al., 2007, 2008b; Hounslow & Nawrocki, 2008). The inability to fully isolate S-class ChRM directions in most inferred reverse polarity specimens is probably due to some stability-overlap between the LT component and the Triassic magnetisation. This overlap of unblocking spectra causes large arc-length great circle trends in reverse polarity specimens, due to the large directional difference (c. 160°) between Triassic reverse polarity and the overprint (i.e., the Brunhes magnetic field; Fig. 7a, b, d). In inferred normal specimens the directional difference between the Brunhes magnetic field and the Triassic normal polarity magnetic field is smaller (c. 20°), and great circle trends are less apparent, and near-straight line-like demagnetisation trajectories dominate (within the measurement uncertainty; Fig. 7c, e, g).

The mean directions of the reverse and normal polarity Triassic directions were determined (Table 1) by combining the great circles (right of Fig. 8) and the S-class ChRM data in the combined great circle analysis of McFadden & McElhinney (1988) (see Hounslow et al., 2007, 2008b for details). The VGP-site-mean, A95 is within the thresholds of Deenen et al. (2011) indicating directional dispersion is within the range of secular variation for all the sections (Table 1). Reversal tests are also positive (class Rb, Rc) for all the three sections, and for all the Hopen data combined (Table 1). The sample set includes a few percent of samples with $\%VGP_{45} <|45°|$ (Table 1), implying a few transitional fields, but these amounts are within the nominal range of 3–4% expected from recent field models (Cromwell et al., 2018).

Polarity stratigraphy

On Hopen, the resulting magnetozone R–N couplets (labelled HO, for Hopen), generated by merging the data from the Nørdstefjellet and Binnedalen sections, are labelled from the oldest parts of the section (HO1r at the base, since by convention normal-reverse couplets start with a normal magnetozone; Fig. 9). Magnetozones defined by a single sampling horizon within an interval of opposite polarity are designated sub-zones. There are seven subzones, HO3r.1n, HO3r.2n, HO4r.1n and the subzones .1r, .2r, .3r and 4r in HO5n. All these are defined by two or more specimens from each sample (Fig. 9). The polarity boundary between magnetozones HO3n and HO3r corresponds to an erosive boundary at the base of Channel Sandstone-2, in the Binnedalen Section, so part of the polarity record is likely missing in the composite height. However, closely spaced samples 2H-14 and 2H-15 in the Binnedalen section display

this boundary (Fig. 6). It is also possible that the condensation or hiatus at the Slottet Bed may have also compressed part of magnetozone HO5r (Fig. 9).

Magnetozones in the Tumlingodden section are labelled Tu, with one major normal magnetozone (TU2n), and two submagnetozones (TU2r.1n and TU2r.2n; Fig. 10). Since the base of TU2n also coincides with a sandstone bed with probable erosive contact on the underlying shale, parts of TU2n and TU1r may have been removed by erosion (Fig. 10). The Slottet Bed is reverse polarity like seen in the Nørdstefjellet section on Hopen, but unlike on Hopen we were not able to extend sampling upwards (due to permafrost) to detect the overlying normal magnetozone like on Hopen.

The reverse-polarity dominated Isfjorden Member at Tumlingodden is clearly not equivalent to the normal-polarity dominated Hopen Member. (Figs. 9 & 10). However, it is rather similar in polarity dominance to the Isfjorden Member. at the Dalsnuten section in central Svalbard (Hounslow et al., 2007), comprising some 64% and 79% of reverse-polarity samples at Dalsnuten and Tumlingodden, respectively.

Carbon isotope stratigraphy

The $\delta^{13}C_{org}$ data from the samples are combined with the data from Paterson et al. (2016) from the Binnedalen and Lyngefjellet sections (Fig. 9a). Their data include a more detailed sampling in the Flatsalen Formation. The combined data show three carbon isotope excursions (CIE), one within the oldest part of the section (around -30 m level) shown by two samples (HO2, HO3) from approximately the same stratigraphic level, but around 80 m apart from the lower part of the cliff in the Nørdstefjellet section (CIE magnitude ca $-4^{0}/_{00}$). For the overlying c. 140 m, $\delta^{13}C_{org}$ is relatively similar. However, the data from Paterson et al. (2016) is displaced by c. $-1^{0}/_{00}$ to lower values, probably due to a lithological contrast in sample types, with the palynological samples biased to shaley intervals, and the paleomagnetic samples biased to sandier lithologies. At c. 125 m is a second CIE (magnitude c. $-4^{0}/_{00}$) which is shown in both the Binnedalen and Nørdstefjellet samples (Fig. 9a). Lastly located at around the Slottet Bed is a smaller amplitude CIE (c. $-2^{0}/_{00}$), shown in the samples from Nørdstefjellet and the samples of Paterson et al. (2016) from the Binnedalen and Lyngefjellet sections.

Discussion

Is there an organic matter compositional control on $\delta^{13}C_{org}$ changes?

The part of the sections with the most marine organic matter is probably around and above the maximum flooding surface (Fig. 9a) inferred in the base of the Flatsalen Formation by Paterson et al. (2016). However, this interval corresponds to the recovery in the $\delta^{13}C_{org}$ data in the Flatsalen Formation (Fig. 9a), so is not clearly related to enhanced marine OM. The sampling of Paterson et al. (2016) is not extensive and detailed enough in the underlying De Geerdalen Formation to identify any short-term major changes in palynofacies, which are instead dominated by terrestrial organic matter (OM) with rather more lacustrine algal components in the Hopen Member. The %C of the samples is not related to $\delta^{13}C_{org}$ (Figs. 9a & 11a) indicating that the isotopic variations are not related to changes in OM concentration, with the $\delta^{13}C_{org}$ excursions ranging from low to high values of %C, like the background values. The background $\delta^{13}C_{org}$ values typically ranging from c.-26 to $-23^{0}/_{00}$ are also typical of the range in terrestrial OM seen in other Late Triassic studies (Fig. 12a).

Terrestrial OM has a larger C/N ratio (elemental ratios used here) compared to marine and

lacustrine organic matter, which has C/N < c. 10 (Fig. 12b). Although its challenging to compare total sediment nitrogen (N_T) with organic matter C/N components (Rau et al., 1987; Middelburg & Nieuwenhuize, 1998; Ogrinc et al., 2005), we estimated an approximate inorganic nitrogen ($\%N_i$) correction to the $\%N_T$ by assuming that $\%N_T$ comprises a linear segment which co-varies with the %C, at higher %C values, and an N_i component which dominates at lower %C values (Fig. 11b; Goñi et al., 1998). The y-axis intercept of the linear %C -related component suggests $\%N_i$ is c. 0.03% (Fig. 11b). This separates the data into two subsets with N_T >0.03% in which the organic matter C/N ratio can be estimated (Fig. 12b), and a subset N_T <0.03% in which it cannot be estimated (Fig. 12c). The former subset shows organic matter C/N ratios which overlap the range of terrestrial OM suggested by Meyers (1994) and Fang et al. (2013), but with a spread towards marine and lacustrine OM with C/N c. 5–10 (Fig. 12b). Some of this scatter in C/N is clearly related to imprecisely estimated N_i (e.g., high C/N >50 at N_T = 0.04%; Fig. 12b; SI Table S3). In the samples, the spread of C/N at <15 is largely from samples below the Hopen Member. (5 out of 6 samples, %C range of 0.23– 1.5%) and may reflect an OM contribution from either marine or lacustrine OM. Paterson et al. (2016) detected minor but regular contributions from fish, ostracods, and agglutinated foraminifera in this part of the Hopen sections, which may be reflecting OM from non-terrestrial sources. A greater contribution of marine organic matter in the shales probably accounts for the minor offset of c. -1‰ between the shale-dominated samples of Paterson et al. (2016) and those we measured focussed on the sandier lithologies, which are likely richer in terrestrial OM. Apart from a single sample at a height of 123 m (%C = 1.5%) in the Binnedalen section (Fig. 12b), the bulk of the samples displaying the CIE's on Hopen have %C <0.4% (Fig. 12c) just like other 'background' $\delta^{13}C_{org}$ samples with similar %C (Figs. 11a & 12c).

Consequently, there is no compelling evidence that the $\delta^{13}C_{org}$ excursions are related to pulses in either enhanced organic matter input, palynological composition, or C/N ratios. This suggests that the CIE's seen in the sections probably reflect rapid input of large amounts of isotopically light carbon into the Triassic ocean-atmosphere to generate the negative CIE's (Saltzman & Thomas, 2012).

Carbon isotope excursions in the late Carnian (Tuvalian) and early Norian (Lacian)

The primary source of reference carbon isotope data for the late Carnian to early Norian is from sections at Pizzo Mondello (PM) and Black Bear Ridge (Figs. 13c, d). Each section has several studies with differing sampling density, but largely focussing on $\delta^{13}C_{carb}$, using either whole-rock analyses or microdrilled samples (to try to bias measurements towards to the micritic limestone components). Only the lower part of the *Metapolygnathus parvus* Zone has $\delta^{13}C_{org}$ data at Black Bear Ridge (Fig. 13d). Additional, $\delta^{13}C_{carb}$ comes from the Silická Brezová section using whole rock and brachiopod calcite (Fig. 13a), and $\delta^{13}C_{org}$ data from the Quingyan Gou section (Fig. 13b). All these sections possess a magnetostratigraphy, apart from Black Bear Ridge (BBR). When taken together these allow the relationship between CIE and magnetozones to be determined in the Tuvalian to early Lacian interval. The magnetostratigraphic correlation between Pizzo Mondello and Silická Brezová follows Muttoni et al. (2004) and Maron et al. (2019). To simplify description, the CIE's have been labelled as Tuvalian negative CIE's (TCIE 1 to 6), starting from the basal Tuvalian CIE (TCIE-1 here) identified by Dal Corso et al. (2018) and labelled by them NCIE-3.

Carbon isotope changes through magnetozone PM4n and PM4r generally display an upwards trend to more positive values (Onoue et al., 2016; Jin et al., 2019), which is shown well in the

Quigyan Gou and Pizzo Mondello sections (Fig. 13b, c). The close-spaced sample sets at PM and BBR suggest that this may be comprised of a brief upper carbon isotope excursion (TCIE-6), which is seen at BBR in $\delta^{13}C_{org}$ and $\delta^{13}C_{carb}$, and a brief lower CIE (TCIE-5) seen in the data of Mazza et al. (2010) at Pizzo Mondello and Lei et al. (2021) at Black Bear Ridge (Fig. 13c, d). At the Quigyan Gou section, these two CIE's seem to be combined into the strong step change in $\delta^{13}C_{org}$ in the late part of the oldest normal magnetozone, equivalent to PM4n (Fig. 13b). TCIE-5 represents the initially most negative part of the transition to more positive values in the lower part of PM4r (and lower *M. parvus* Zone). Above TCIE-6 is a broad positive CIE, followed by a negative excursion approximately near the top of the *M. parvus* Zone (Lacian CIE-1; Fig. 13c, d). LCIE-1 is clearly seen within magnetozone PM5n (at Pizzo Mondello) and the equivalent magnetozone at Quigyan Gou. At BBR, excursion LCIE-1 is within the lower part of the Kerri Zone and around the FO of *Halobia austriaca* (i.e., base of the Norian) in both the PM and the BBR sections.

Within magnetozone PM2r (at Pizzo Mondello) and the equivalent magnetozone at Silická Brezová is isotope excursion TCIE-4. Ammonoids from this level at PM place this in the *Discotropites plinii* Subzone (Tuvalian- 3, (I) sub-interval; Balini et al., 2012). Since the Macrolobatus Zone of British Columbia correlates to the upper part of the Spinosus Zone (Tuvalian-3; Balini et al., 2010), it is most likely that TCIE-4 represents the CIE in the uppermost part of the Welleri Zone at BBR (Fig. 13d).

Reconstructing the likely carbon isotope excursions in the mid and lower Tuvalian is less certain. Dal Corso et al. (2018) identified a CIE in the early part of Tuvalian-2 (in the base of the Travenanzes Formation of the Dibona Section), which is possibly that seen at Silická Brezová and labelled TCIE-2. The additional CIE seen in the base of the PM section is around the Tuvalian-2 to Tuvalian-3 boundary (labelled as TCIE-3) which is an ill-defined boundary in all these sections.

Placing the Carnian–Norian boundary in the Svalbard successions

The $\delta^{13}C_{org}$ excursions seen in the Hopen sections, combined with the magnetostratigraphy, allows a precise correlation to the Pizzo Mondello and Silická Brezová sections. At the base of the Hopen sections, TCIE-4 is likely that seen within the magnetozone HO1r, and the equivalent PM2r magnetozone in other sections (Fig. 14). Magnetozone PM2r (and HO1r) is equivalent to UT10r in the magnetochron composite of Hounslow & Muttoni (2010) and Newark Supergroup magnetozone E5r in the composite of Maron et al. (2019).

The CIE in the Hopen Member, within the normal magnetozone HO5n, is likely to be TCIE-5, within magnetozone PM4n at Pizzo Mondello (Fig. 14; UT12n in composite), and its correlatives in other sections (Fig. 13). This occurs above a long interval of relatively consistent $\delta^{13}C$ in all these sections (Figs. 13d & 14). Whilst TCIE-5 is not so distinct at PM, it is clearly shown as a brief sharp excursion at BBR with a magnitude of c. -1.5‰ (Fig. 13d).

The smaller negative CIE centred on the Slottet Bed shows an overlying slow recovery through the lowest part of the Flatsalen Formation, through an interval of normal polarity (equivalent to UT13n magnetochron; Fig. 14). Since TCIE-6 at PM shows this recovery within PM4r (UT12r magnetochron), it is likely this CIE on Hopen is condensed (or truncated), with the lower part of UT13n, so that the upper part of UT13n which contains LCIE-1, sits on UT12r (marked as missing Hopen interval in Fig. 14). The uppermost reverse-polarity sample from HO5r (at the Nørdstefjellet section; Fig. 6) is in the upper part of the Slottet Bed (above an erosional contact within the bed), so it would seem the missing (or highly condensed) part may be in the lowest, unsampled ~5 m of the Flatsalen Formation

on Hopen. The Carnian–Norian boundary is therefore close to the base of the Flatsalen Formation (or in its basal few meters) above the Slottet Bed. A cm-scale carbon isotope profile in this interval on Hopen may allow a more precise placement of the boundary.

Conclusions

A detailed sampling of two sections on Hopen and one on Wilhelmøya has allowed a more detailed understanding of the chronostratigraphic relationships of the Tuvalian and Lacian Substages (late Carnian to early Norian) to the Svalbard lithostratigraphy. This has been gained through a magnetostratigraphic study linked to new and existing organic carbon isotope data. The organic carbon isotope data is demonstrated to be little impacted by changes in the composition of organic matter, so likely reflects global perturbations in light carbon inputs.

A re-evaluation of existing Tuvalian to earliest Lacian carbon isotope data from Tethyan and Canadian sections, suggests that six negative carbon excursions exist in the Tuvalian (TCIE 1 to TCIE-6), and one in the earliest Lacian (LCIE-1), briefly following the base of the Norian. All of these excursions, except TCIE-3, are currently represented in the Carnian– early Norian successions on Svalbard. The association of the CIE with the magnetostratigraphy strengthens support for the proposed age model of the upper part of the De Geerdalen Formation. A revised polarity pattern through the entire Tuvalian (Fig. 14) is also proposed filling the 'mid-Carnian gap' in magnetostratigraphic data.

The base of the Norian is located at the base or lowermost few metres of the Flatsalen Formation on Hopen, and only a small part of the latest Tuvalian appears to be missing on Hopen. Based on the magnetic polarity stratigraphy, and carbon isotope data, the Isfjorden Member from central Spitsbergen and NE Svalbard is likely early Tuvalian-2 in age, suggesting a major hiatus at the base of the Wilhelmøya Subgroup on Spitsbergen and Wilhelmøya. This hiatus likely corresponds with much of the regressive part of sequence S5 of Klausen et al. (2015).

Acknowledgements. We thank all participants on the different Hopen expeditions. Gareth Lord helped collect some of these samples and allowed use of the log from Tumlingodden. Victoria Lucas measured some of the magnetic data. David Mindham pre-processed the samples for $\delta^{13}C$, that were measured by Dave Hughes at Lancaster. This work was part-funded through the Hopen Study Group by a range of funding partners. The reviewer Snorre Olaussen provided much constructive comment.

References

Anell, I.M., Braathen, A. & Olaussen, S., 2014: The Triassic–Early Jurassic of the northern Barents Shelf: a regional understanding of the Longyearbyen CO_2 reservoir. *Norwegian Journal of Geology 94*, 83–98.

Bacon, K.L., Belcher, C.M., Hesselbo, S.P. & Mcelwain, J.C. 2011: The Triassic–Jurassic boundary carbon-isotope excursions expressed in taxonomically identified leaf cuticles. *Palaios 26*, 461–469. https://doi.org/10.2110/palo.2010.p10-120r

Balini, M., Lucas, S.G., Jenks, J.F. & Spielmann, J.A. 2010: Triassic ammonoid

biostratigraphy: an overview. *In:* Lucas, S.G. (ed.) *The Triassic timescale*. Geological Society, London, Special Publications *334*, pp.221–262. https://doi.org/10.1144/SP334.10

Balini, M., Krystyn, L., Levera, M. & Tripodo, A., 2012: Late Carnian–Early Norian ammonoids from the GSSP candidate section Pizzo Mondello (Sicani Mountains, Sicily). *Rivista italiana di paleontologia e stratigrafia 118*. 47–84.

Bragin, N.Y, Konstantinov, A.G., & Sobolev E. S. 2012: Upper Triassic Stratigraphy and Paleobiogeography of Kotel'nyi Island (New Siberian Islands). *Stratigraphy and Geological Correlation 20*, 541–566. https://doi.org/10.1134/S0869593812050036

Briden, J.C. & Arthur, G.R., 1981: Precision of measurement of remanent magnetization. *Canadian Journal of Earth Sciences 18,* 527–538. https://doi.org/10.1139/e81-046

Brodie, C.R., Leng, M.J., Casford, J.S., Kendrick, C.P., Lloyd, J.M., Yongqiang, Z. & Bird, M.I. 2011: Evidence for bias in C and N concentrations and $\delta^{13}C$ composition of terrestrial and aquatic organic materials due to pre-analysis acid preparation methods. *Chemical Geology 282*, 67–83. https://doi.org/10.1016/j.chemgeo.2011.01.007

Broglio Loriga, C., Cirilli, S., De Zanche, V., di Bari, D., Gianolla, P., Laghi, G. F., Lowrie, W., Manfrin, S., Mastandrea, A., Mietto, P., Muttoni, G., Neri, C., Posenato, P., Rechichi, M., Rettori, R. & Roghi, G. 1999: The Prati di Stuores/Stuores Wiesen section (Dolomites, Italy): a candidate Global Stratotype Section and Point for the base of the Carnian stage: *Rivista Italiana di Paleontologia e Stratigrafia 105*, 37–78.

Channell, J.E.T., Kozur, H.W., Sievers, T., Mock, R., Aubrecht, R. & Sykora, M. 2003: Carnian–Norian biomagnetostratigraphy at Silická Brezová (Slovakia): correlation to other Tethyan sections and to the Newark Basin. *Palaeogeography, Palaeoclimatology, Palaeoecology 191*, 65–109. https://doi.org/10.1016/S0031-0182(02)006545

Cirilli, S. 2010: Upper Triassic–lowermost Jurassic palynology and palynostratigraphy: a review. *In*: S.G. Lucas (ed.) *The Triassic time scale*. Geological Society, London, Special Publications, 334. pp. 285–314. https://doi.org/10.1144/SP334.12

Cromwell, G., Johnson, C.L., Tauxe, L., Constable, C.G. & Jarboe, N.A., 2018: PSV10: A global data set for 0–10 Ma time-averaged field and paleosecular variation studies. *Geochemistry, Geophysics, Geosystems 19*, 1533–1558. https://doi.org/10.1002/2017GC007318

Dagys, A. S. & Weitschat, W. 1993: Correlation of the Boreal Triassic. *Mitteilungen Geologisch-Paläontologisches Institut Universität Hamburg 75*, 249–256.

589 Dal Corso, J., Mietto, P., Newton, R.J., Pancost, R.D., Preto, N., Roghi, G. & Wignall, P.B.
590 2012: Discovery of a major negative δ13C spike in the Carnian (Late Triassic) linked to the
591 eruption of Wrangellia flood basalts. *Geology 40*, 79–82. https://doi.org/10.1130/G32473.1

592

593 Dal Corso, J., Gianolla, P., Rigo, M., Franceschi, M., Roghi, G., Mietto, P., Manfrin, S.,
594 Raucsik, B., Budai, T., Jenkyns, H.C. & Reymond, C.E. 2018: Multiple negative carbon-
595 isotope excursions during the Carnian Pluvial Episode (Late Triassic). *Earth-Science Reviews*
596 *185*, 732–750. https://doi.org/10.1016/j.earscirev.2018.07.004

597

598 Deenen, M.H., Langereis, C.G., van Hinsbergen, D.J. & Biggin, A.J. 2011: Geomagnetic
599 secular variation and the statistics of palaeomagnetic directions. *Geophysical Journal*
600 *International 186*, 509–520. https://doi.org/10.1111/j.1365-246X.2011.05050.x

601

602 Deenen, M.H., Langereis, C.G., van Hinsbergen, D.J. & Biggin, A.J., 2014: Erratum:
603 Geomagnetic secular variation and the statistics of palaeomagnetic directions. *Geophysical*
604 *Journal International 197,* 643–643. https://doi.org/10.1093/gji/ggu021

605

606 Fang, L., Bjerrum, C.J., Hesselbo, S.P., Kotthoff, U., McCarthy, F.M., Huang, B. &
607 Ditchfield, P.W. 2013: Carbon-isotope stratigraphy from terrestrial organic matter through
608 the Monterey event, Miocene, New Jersey margin (IODP Expedition 313). *Geosphere 9*,
609 1303–1318.

610

611 Gallet, Y., Besse, J., Krystyn, L., Marcoux, J. & Theveniaut, H. 1992: Magnetostratigraphy
612 of the Late Triassic Bolücektasi Tepe section (southwestern Turkey): Implications for
613 changes in magnetic reversal frequency. *Physics of the Earth and Planetary Interiors 73*, 85–
614 108. https://doi.org/10.1016/0031-9201(92)90109-9

615

616 Gallet, Y., Besse, J., Krystyn, L., Théveniaut, H. & Marcoux, J. 1994: Magnetostratigraphy
617 of the Mayerling section (Austria) and Erenkolu Mezarlik (Turkey) section: Improvement of
618 the Carnian (Late Triassic) magnetic polarity time scale. *Earth and Planetary Science Letters*
619 *125*, 173–191. https://doi.org/10.1016/0012-821X(94)90214-3

620

621 Gallet, Y., Krystyn, L. & Besse, J. 1998: Upper Anisian to Lower Carnian
622 magnetostratigraphy from the Northern Calcareous Alps (Austria). *Journal of Geophysical*
623 *Research 103*, 605–621. https://doi.org/10.1029/97JB02155

624

625 Gallet, Y., Besse, J., Krystyn, L., Marcoux, J., Guex, J. & Théveniaut, H. 2000:
626 Magnetostratigraphy of the Kavaalani section (southwestern Turkey): Consequence for the
627 origin of the Antalya Calcareous Nappes (Turkey) and for the Norian (Late Triassic)
628 magnetic polarity timescale. *Geophysical Research Letters 27*, 2033–2036.
629 https://doi.org/10.1029/2000GL008504

630

631 Gallet, Y., Krystyn, L., Besse, J. & Marcoux, J. 2003: Improving the Upper Triassic
632 numerical timescale from cross-correlation between Tethyan marine sections and the
633 continental Newark Basin sequence. *Earth and Planetary Science Letters 212*, 255–261.
634 https://doi.org/10.1016/S0012-821X(03)00290-5

635

636 Gilmullina, A., Klausen, T.G., Paterson, N.W., Suslova, A. & Eide, C.H. 2021: Regional
637 correlation and seismic stratigraphy of Triassic Strata in the Greater Barents Sea:
638 Implications for sediment transport in Arctic basins. *Basin Research 33*, 1546–1579.
639 https://doi.org/10.1111/bre.12526

640

641 Glørstad-Clark, E., Faleide, J.I., Lundschien, B.A. & Nystuen, J.P. 2010: Triassic seismic
642 sequence stratigraphy and palaeogeography of the western Barents Sea area. *Marine and*
643 *Petroleum Geology 27*, 1448–1475. https://doi.org/10.1016/j.marpetgeo.2010.02.008

644

645 Goñi, M.A., Ruttenberg, K.C. & Eglinton, T.I. 1998: A reassessment of the sources and
646 importance of land-derived OM in surface sediments from the Gulf of Mexico. *Geochim.*
647 *Cosmochim. Acta 62*, 3055– 3075. https://doi.org/10.1016/S0016-7037(98)00217-8

648

649 Haile, B.G., Czarniecka, U., Xi, K., Smyrak-Sikora, A., Jahren, J., Braathen, A. & Hellevang,
650 H. 2019: Hydrothermally induced diagenesis: Evidence from shallow marine-deltaic
651 sediments, Wilhelmøya, Svalbard. *Geoscience Frontiers*, 10, 629–649.
652 https://doi.org/10.1016/j.gsf.2018.02.015

653

654 Harland, W.B. 1997: *Svalbard, Chapter 18, Triassic history*. Geological Society, London,
655 Memoirs, 17, pp. 340–362. https://doi.org/10.1144/GSL.MEM.1997.017.01.18

656

657 Haugen, T. 2016: *A sedimentological study of the De Geerdalen Formation with focus on the*
658 *Isfjorden Member and palaeosols.* Master's thesis, NTNU, Trondheim, 151 pp.

659

660 Hochuli, P. A., Colin, J. P. & Vigran, J. O. 1989: Triassic biostratigraphy of the Barents Sea
661 area. *In*: Collinson, J. D. (ed), *Correlation in Hydrocarbon Exploration*, Norwegian
662 Petroleum Society, Graham & Trotman, 131–153. https://doi.org/10.1007/978-94-009-1149-
663 9_12

664

665 Hounslow, M.W. 2006: PMagTools version 4.2- a tool for analysis of 2-D and 3-D
666 directional data.

667

668 Hounslow, M.W. & Muttoni, G. 2010: The Geomagnetic Polarity Timescale for the Triassic:
669 linkage to stage boundary definitions. *In* Lucas S.G. (ed.): *The Triassic time scale*, Special
670 Publication Geological Society 334, pp. 61–102. https://doi.org/10.1144/SP334.4

671

672 Hounslow, M.W & Nawrocki, J. 2008: Palaeomagnetism and magnetostratigraphy of the

673 Permian and Triassic of Spitsbergen: a review of progress and challenges. *Polar Research 27*,
674 502–522. https://doi.org/10.1111/j.1751-8369.2008.00075.x

675 Hounslow, M.W., Hu, M., Mørk, A., Vigran, J.O., Weitschat, W. & Orchard M.J. 2007:
676 Magneto-biostratigraphy of the lower part of the Kapp Toscana Group (Carnian),
677 Vendomdalen, central Spitsbergen, arctic Norway. *Journal of the Geological Society,*
678 *London, 164,* 581–597. https://doi.org/10.1144/0016-76492005-184

679

680 Hounslow, M.W., Peters, C., Mørk, A., Weitschat, W. & Vigran, J.O. 2008a: Bio-
681 magnetostratigraphy of the Vikinghøgda Formation, Svalbard (arctic Norway) and the
682 geomagnetic polarity timescale for the Lower Triassic. *Geological Society of America*
683 *Bulletin 120*, 1305–1325. https://doi.org/10.1130/B26103.1

684

685 Hounslow, M.W., Hu, M., Mørk, A., Weitschat, W., Vigran, J.O., Karloukovski, V. &
686 Orchard, M.J. 2008b: Intercalibration of Boreal and Tethyan timescales: the magneto-
687 biostratigraphy of the Middle Triassic and the latest Early Triassic, central Spitsbergen (arctic
688 Norway). *Polar Research 27*, 469–490. https://doi.org/10.1111/j.1751-8369.2008.00074.x

689

690 Hounslow, M.W., Harris, S.E., Wójcik, K., Nawrocki, J., Ratcliffe, K.T., Woodcock, N.H. &
691 Montgomery, P., 2021a: A geomagnetic polarity stratigraphy for the Middle and Upper
692 Ordovician. *Palaeogeography, Palaeoclimatology, Palaeoecology 567*,
693 https://doi.org/10.1016/j.palaeo.2021.110225

694

695 Hounslow, M.W, Bachmann, G.H, Balini, M., Benton, M.J., Carter, E.S., Konstantinov,
696 A.G., Golding, M.L., Krystyn, L., Kuerschner, W., Lucas, S.G., McRoberts, C.A., Muttoni,
697 G., Nicora, A., Onoue, T., Orchard, M.J., Ozsvárt, P., Paterson, N.W., Richoz, S., Rigo, M.,
698 Sun, Y., Tackett, L.S., Tekin, U.K., Wang, Y., Zhang, Y. & Zonneveld, J.P. 2021b: The case
699 for the global stratotype and section and point (GSSP) for the base of the Norian Stage.
700 *Albertiana*, 46, 25–57.

701

702 Jin, X., McRoberts, C.A., Shi, Z., Mietto, P., Rigo, M., Roghi, G., Manfrin, S., Franceschi,
703 M. & Preto, N. 2019: The aftermath of the CPE and the Carnian–Norian transition in
704 northwestern Sichuan basin, South China. *Journal of the Geological Society 176*, 179–196.
705 https://doi.org/10.1144/jgs2018-104

706

707 Kent, D.V., Olsen, P.E. & Muttoni, G., 2017: Astrochronostratigraphic polarity time scale
708 (APTS) for the Late Triassic and Early Jurassic from continental sediments and correlation
709 with standard marine stages. *Earth-Science Reviews 166*, 153–180.
710 https://doi.org/10.1016/j.earscirev.2016.12.014

711

712 Kent, J.T., Briden, J.C. & Mardia, K.V. 1983: Linear and planar structure in ordered
713 multivariate data as applied to progressive demagnetisation of palaeomagnetic remanence.
714 *Geophysical Journal of the Royal Astronomical Society 81*, 75–87.
715 https://doi.org/10.1111/j.1365-246X.1983.tb05001.x

716

717 Klausen, T.G., Ryseth, A.E., Helland-Hansen, W., Gawthorpe, R., and Laursen, I., 2015,
718 Regional development and sequence stratigraphy of the Middle to Late Triassic Snadd
719 Formation, Norwegian Barents Sea. *Marine and Petroleum Geology 62,* 102–122.
720 https://doi.org/10.1016/j.marpetgeo.2015.02.004

721

722 Konstantinov, A.G. 2014: Zonal correlation and boundaries of the lower Carnian Substage in
723 Northeastern Asia. *Stratigraphy and Geological Correlation 22*, 190–201.
724 https://doi.org/10.1134/S0869593814020051

725

726 Konstantinov, A. G. & Sobolev, 2000: Biostratigraphic Scheme of the Carnian and Lower
727 Norian in NE Russia. Paper 2. *New Zonal Scales and Correlation*. Geology of the Pacafic
728 Ocean, 16, pp. 643–666, Harwood Academic Publishers.

729

730 Konstantinov A.G. & Klets T.V. 2009: Stage Boundaries of the Triassic in Northeast Asia.
731 *Stratigraphy and Geological Correlation 17,* 173–191.
732 https://doi.org/10.1134/S0869593809020063

733

734 Konstantinov, A.G., Sobolev, E.S. & Klets, T.V. 2003: New data on fauna and
735 biostratigraphy on Norian deposits in the Kotel'nyi Island (New Siberian Islands).
736 *Stratigraphy and Geological Correlation 11*, 231–243.

737

738 Korčinskaya, M.V. 1980: *Early Norian Fauna of the Archipelago of Svalbard*. *Geologiya*
739 *osadochnogo chekhla arkhipelaga Sval'bard* (Geology of the Sedimentary Cover of the
740 Archipelago of Svalbard), Leningrad: NIIGA, 30–43. (In Russian).

741

742 Korte, C., Kozur, H.W. & Veizer, J. 2005: $\delta^{13}C$ and $\delta^{18}O$ values of Triassic brachiopods and
743 carbonate rocks as proxies for coeval seawater and Palaeotemperature. *Palaeogeography,*
744 *Palaeoclimatology, Palaeoecology 226*, 287–306. https://doi.org/10.1016/j.palaeo.2005.05.018

745

746 Krystyn, L. 1980: Triassic conodont localities of the Salzkammergut region (northern
747 Calcareous Alps). *In:* H.P. Schönlaub (ed.), *Second European Conodont Symposium,*
748 *Guidebook and Abstracts.* Abhandlungen der Geologischen Bundesanstalt, 35, pp. 61–98.

749

750 Krystyn, L., Gallet, Y., Besse, J. & Marcoux, J. 2002: Integrated Upper Carnian to Lower
751 Norian biochronology and implications for the Upper Triassic magnetic polarity time scale.
752 *Earth and Planetary Science Letters 203*, 343–351. https://doi.org/10.1016/S0012-
753 821X(02)00858-0

754

755 Larson T.E. Heikoop, J.M., Perkins, G., Chipera, S.J. & Hess, M.A. 2008: Pretreatment
756 technique for siderite removal for organic carbon isotope and C:N ratio analysis. *Rapid*
757 *Communications in Mass Spectrometry 22*, 865–872. https://doi.org/10.1002/rcm.3432

758

759 Lei, J.Z.X., Husson, J.M., Golding, M.L., Orchard, M.J. & Zonneveld, J.-P. 2021: Stable
760 carbon isotope record of carbonate across the Carnian–Norian boundary at the prospective
761 GSSP section at Black Bear Ridge, British Columbia, Canada. *Albertiana 46*, 1–10.

762

763 Lord, G., Solvi, K.H., Ask, M., Mørk, A., Hounslow, M.W. & Paterson, N.W. 2014: The
764 Hopen member: a new member of the Triassic de Geerdalen formation. *Norwegian*
765 *Petroleum Directorate Bulletin 11*, 81–96.

766

767 Lord, G.S., Johansen, S.K., Støen, S.J. & Mørk, A. 2017: Facies development of the Upper
768 Triassic succession on Barentsøya, Wilhelmøya and NE Spitsbergen, Svalbard. *Norwegian*
769 *Journal of Geology 97*, 33–62. https://doi.org/10.17850/njg97-1-03

770

771 Lord, G.S., Mørk, M.B.E., Mørk, A. & Olaussen, S. 2019: Sedimentology and petrography of
772 the Svenskøya Formation on Hopen, Svalbard: an analogue to sandstone reservoirs in the
773 Realgrunnen Subgroup. *Polar Research 38*. https://doi.org/10.33265/polar.v38.3523

774

775 Maron, M., Muttoni, G., Dekkers, M.J., Mazza, M., Roghi, G., Breda, A., Krijgsman, W. &
776 Rigo, M. 2017: Contribution to the magnetostratigraphy of the Carnian: new magneto-
777 biostratigraphic constraints from Pignola-2 and Dibona marine sections, Italy. *Newsletters in*
778 *Stratigraphy 50*, 187–203. https://doi.org/10.1127/nos/2017/0291

779

780 Maron, M., Muttoni, G., Rigo, M., Gianolla, P. & Kent, D.V. 2019: New
781 magnetobiostratigraphic results from the Ladinian of the Dolomites and implications for the
782 Triassic geomagnetic polarity timescale. *Palaeogeography, Palaeoclimatology,*
783 *Palaeoecology 517*, 52–73. https://doi.org/10.1016/j.palaeo.2018.11.024

784

785 Mazza, M., Furin, S., Spötl, C. & Rigo, M. 2010: Generic turnovers of Carnian/Norian
786 conodonts: Climatic control or competition? *Palaeogeography, Palaeoclimatology,*
787 *Palaeoecology 290*, 120–137. https://doi.org/10.1016/j.palaeo.2009.07.006

788

789 Meyers, P.A. 1994: Preservation of elemental and isotopic source identification of
790 sedimentary organic matter. *Chemical geology 114*, 289–302. https://doi.org/10.1016/0009-
791 2541(94)90059-0

792

793 McFadden, P. L. & McElhinny, M. W. 1988: The combined analysis of remagnetisation
794 circles and direct observations in palaeomagnetism. *Earth Planetary Science Letters 87*, 161–
795 172. https://doi.org/10.1016/0012-821X(88)90072-6

796

797 McFadden, P.L. & McElhinny, M.W. 1990: Classification of the reversal test in
798 palaeomagnetism. *Geophysical Journal International 103*, 725–729.
799 https://doi.org/10.1111/j.1365-246X.1990.tb05683.x

800

801 Mietto, P., Manfrin, S., Preto, N, Rigo, M. Roghi, G., Furin, S., Gianolla, P., Posenato, R.,
802 Muttoni, G., Nicora, A., Buratti, N., Cirilli, S., Spötl, C, Ramezani, J., & Bowring, S.A. 2012:
803 The Global Boundary Stratotype Section and Point (GSSP) of the Carnian Stage (Late
804 Triassic) at Prati Di Stuores/Stuores Wiesen Section (Southern Alps, NE Italy). *Episodes 35*,
805 414–430. https://doi.org/10.18814/epiiugs/2012/v35i3/003

806

807 Middelburg, J.J. & Nieuwenhuize, J. 1998: Carbon and nitrogen stable isotopes in suspended
808 matter and sediments from the Schelde Estuary. *Marine Chemistry*, *60*, 217–225.
809 https://doi.org/10.1016/S0304-4203(97)00104-7

810

811 Mueller, S., Hounslow, M.W. & Kürschner, W.M. 2016: Integrated stratigraphy and
812 palaeoclimate history of the Carnian Pluvial Event in the Boreal realm; new data from the
813 Upper Triassic Kapp Toscana Group in central Spitsbergen (Norway). *Journal of the*
814 *Geological Society 173*, 186–202. https://doi.org/10.1144/jgs2015-028

815

816 Muttoni, G., Kent, D.V., Olsen, P.E., Stefano, P.D., Lowrie, W., Bernasconi, S.M. &
817 Hernández, F.M. 2004: Tethyan magnetostratigraphy from Pizzo Mondello (Sicily) and
818 correlation to the Late Triassic Newark astrochronological polarity time scale. *Geological*
819 *Society of America Bulletin 116*, 1043–1058. https://doi.org/10.1130/B25326.1

820

821 Muttoni, G., Mazza, M., Mosher, D., Katz, M.E., Kent, D.V. & Balini, M. 2014: A Middle–
822 Late Triassic (Ladinian–Rhaetian) carbon and oxygen isotope record from the Tethyan
823 Ocean. *Palaeogeography, Palaeoclimatology, Palaeoecology 399*, 246–259.
824 https://doi.org/10.1016/j.palaeo.2014.01.018

825

826 Mørk, A. & Worsley, D. 2006: Triassic of Svalbard and the Barents Shelf. *In:* Nakrem, H.A.
827 & Mørk, A. (eds.) *Boreal Triassic 2006*. NGF, Abstracts and Proceedings of the Geological
828 Society of Norway, 3.

829

830 Mørk, A., Knarud, R. & Worsley, D. 1982: Depositional and diagenetic environments of the
831 Triassic and Lower Jurassic succession of Svalbard. *In*: Embry, A.F. & Balkwill, H. R. (eds),
832 *Arctic Geology and Geophysics*, Canadian Society of Petroleum Geologists, Memoir 8, pp.
833 371–398.

834

835 Mørk, A., Vigran, J.O. & Hochuli, P.A. 1990: Geology and palynology of the Triassic
836 succession of Bjørnøya. *Polar Research 8*, 141–163. https://doi.org/10.3402/polar.v8i2.6810

837

838 Mørk, A., Dallmann, W.K., Dypvik, H., Johannessen, E.P., Larssen, G.B., Nagy, J., Nøttvedt,
839 A., Olaussen, S., Pchelina, T.M. & Worsley, D. 1999: Mesozoic lithostratigraphy. *In:*
840 Dallmann, W.K. (Ed.), *Lithostratigraphic lexicon of Svalbard. Review and recommendations*
841 *for nomenclature use*: Upper Palaeozoic to Quaternary bedrock. Norsk Polarinstitutt, Tromsø,
842 pp. 127–214.

843

Mørk, A., Lord, G.S., Solvi, K.H. & Dallmann, W.K. 2013: *Geological Map of Svalbard*, sheet G14G Hopen, scale 1:100,000, Norsk Polarinstitutt Temakart 50.

Mørk, M.B.E. 1999: Compositional variations and provenance of Triassic sandstones from the Barents Shelf. *Journal of Sedimentary Research 69*, 690–710. https://doi.org/10.2110/jsr.69.690

Nagy, J., Hess, S., Dypvik, H. and Bjærke, T., 2011: Marine shelf to paralic biofacies of Upper Triassic to Lower Jurassic deposits in Spitsbergen. *Palaeogeography, Palaeoclimatology, Palaeoecology 300*, 138–151. https://doi.org/10.1016/j.palaeo.2010.12.018

Ogrinc, N., Fontolan, G., Faganeli, J. & Covelli, S. 2005: Carbon and nitrogen isotope compositions of organic matter in coastal marine sediments (the Gulf of Trieste, N Adriatic Sea): indicators of sources and preservation. *Marine chemistry 95*, 163–181. https://doi.org/10.1016/j.marchem.2004.09.003

Opdyke, N.D & Channel, J.E.T. 1996: *Magnetic Stratigraphy*, Acedemic press, London, 346pp.

Onoue, T., Zonneveld, J.P., Orchard, M.J., Yamashita, M., Yamashita, K., Sato, H. & Kusaka, S. 2016: Paleoenvironmental changes across the Carnian/Norian boundary in the Black Bear Ridge section, British Columbia, Canada. *Palaeogeography, Palaeoclimatology, Palaeoecology 441*, 721–733. https://doi.org/10.1016/j.palaeo.2015.10.008

Orchard, M.J. 2010: Triassic conodonts and their role in stage boundary definition. *In:* Lucas, S.G. (ed.) *The Triassic timescale. Geological Society, London, Special Publications*, 334, pp. 139–162. https://doi.org/10.1144/SP334.7

Paterson, N.W. & Mangerud, G. 2015: Late Triassic (Carnian–Rhaetian) palynology of Hopen, Svalbard. *Review of Palaeobotany and Palynology 220*, 98–119. https://doi.org/10.1016/j.revpalbo.2015.05.001

Paterson, N.W. & Mangerud, G. 2020: A revised palynozonation for the Middle–Upper Triassic (Anisian–Rhaetian) Series of the Norwegian Arctic. *Geological Magazine 157*, 1568–1592. https://doi.org/10.1017/S0016756819000906

Paterson, N.W., Mangerud, G., Cetean, C.G., Mørk, A., Lord, G.S., Klausen, T.G. & Mørkved, P.T., 2016: A multidisciplinary biofacies characterisation of the Late Triassic (late Carnian–Rhaetian) Kapp Toscana Group on Hopen, Arctic Norway. *Palaeogeography, Palaeoclimatology, Palaeoecology 464*, 16–42. https://doi.org/10.1016/j.palaeo.2015.10.035

Pčelina, T.M., 1972: K voprosu o vozraste osadočnoj tolšči ostrova Nadeždy (Sval'bard) (On

the question of the age of sedimentary succession of the island of Hopen (Svalbard)). *In:* Sokolov, V.N., Vasilevskaya, N.D. (Eds.), *Mezozoiskie otloženija Sval'barda. (Mesozoic deposits of Svalbard).* N.I.I.G.A, Leningrad, pp. 75–81 (In Russian).

Rau, G.H., Arthur, M.A. & Dean, W.E. 1987: $^{15}N/^{14}N$ variations in Cretaceous Atlantic sedimentary sequences: Implication for past changes in marine nitrogen biogeochemistry. *Earth and Planetary Science Letters 82*, 269–279. https://doi.org/10.1016/0012-821X(87)90201-9

Riis, F., Lundschien, B.A., Høy, T. Mørk, A. & Mørk, M.B. 2008: Evolution of the Triassic shelf in the northern Barents Sea region. *Polar Research 27*, 318–338. https://doi.org/10.1111/j.1751-8369.2008.00086.x

Rismyhr, B., Bjærke, T., Olaussen, S., Mulrooney, M.J. & Senger, K. 2018: Facies, palynostratigraphy and sequence stratigraphy of the Wilhelmøya Subgroup (Upper Triassic–Middle Jurassic) in western central Spitsbergen, Svalbard. *Norwegian Journal of Geology* 99, 35–64. https://doi.org/10.17850/njg001

Saltzman, M. R. & Thomas, E. 2012: Carbon isotope stratigraphy. *In:* Gradstein, F. M., Ogg, J.G., Schmitz, M. & Ogg. G. (eds.). *The geologic time scale*, pp. 207–232, Amsterdam: Elsevier. https://doi.org/10.1016/B978-0-444-59425-9.00011-1

Schaller, M.F., Wright, J.D. & Kent, D.V. 2015: A 30 Myr record of Late Triassic atmospheric pCO_2 variation reflects a fundamental control of the carbon cycle by changes in continental weathering. *GSA Bulletin 127*, 661–671. https://doi.org/10.1130/B31107.1

Smith, D.G. Harland, W.B. & Hughes, N.F. 1975: Geology of Hopen, Svalbard. *Geological Magazine 112*, 1–112. https://doi.org/10.1017/S0016756800045544

Smith, D.G. 1982: Stratigraphic significance of a palynoflora from ammonoid- bearing Early Norian strata in Svalbard. *Newsletters in Stratigraphy 11,* 154–161. https://doi.org/10.1127/nos/11/1982/154

Solvi, K.H. 2013: *Visualize and interpret the geometry heterogeneity and lateral continuation of channel bodies in the De Geerdalen Formation at Hopen*. Msc, NTNU, Trondheim, pp. 106.

Twichell, S.C., Meyers, P.A. & Diester-Haass, L. 2002: Significance of high C/N ratios in organic-carbon-rich Neogene sediments under the Benguela Current upwelling system. *Organic Geochemistry 33*, 715–722. https://doi.org/10.1016/S0146-6380(02)00042-6

Vigran, J.O., Mangerud, G., Mørk, A., Worsley, D. & Hochuli, P.A. 2014: Palynology and

geology of the Triassic succession of Svalbard and the Barents Sea. *Geological Survey of Norway Special Publication 14*, 1–247.

Ward, P.D., Garrison, G.H., Williford, K.H., Kring, D.A., Goodwin, D., Beattie, M.J. & McRoberts, C.A. 2007: The organic carbon isotopic and paleontological record across the Triassic–Jurassic boundary at the candidate GSSP section at Ferguson Hill, Muller Canyon, Nevada, USA. *Palaeogeography, Palaeoclimatology, Palaeoecology 244*, 281–289. https://doi.org/10.1016/j.palaeo.2006.06.042

Williford, K.H., Ward, P.D., Garrison, G.H. & Buick, R., 2007a: An extended organic carbon-isotope record across the Triassic–Jurassic boundary in the Queen Charlotte Islands, British Columbia, Canada. *Palaeogeography, Palaeoclimatology, Palaeoecology 244*, 290–296. https://doi.org/10.1016/j.palaeo.2006.06.032

Williford K.A., Orchard, M.J., Zonneveld, J.P. McRoberts, C.A. & Beatty, T.W. 2007b: A record of stable organic carbon isotopes from the Carnian Norian boundary section at Black Bear Ridge, Williston Lake, British Columbia, Canada. *Albertiana 36*, 146–148.

Whiteside, J.H., Olsen, P.E., Eglinton, T., Brookfield, M.E. & Sambrotto, R.N. 2010: Compound-specific carbon isotopes from Earth's largest flood basalt eruptions directly linked to the end-Triassic mass extinction. *Proceedings of the National Academy of Sciences 107*, 6721–6725. https://doi.org/10.1073/pnas.1001706107

Worsley, D. 1973: The Wilhelmøya Formation – a new lithostratigraphic unit from the Mesozoic of Eastern Svalbard. *Norsk Polarinstitutt Årbok* 1971, 7–16.

Zakharov, Y.D. 1997: Carnian and Norian sirenitid ammonoids of the NW circum-Pacific and their role in the Late Triassic faunal successions. *Memoires de Geologie (Lausanne) 30*, 137–144.

Zhang, Y., Li, M., Ogg, J.G., Montgomery, P., Huang, C., Chen, Z.Q., Shi, Z., Enos, P. & Lehrmann, D.J. 2015: Cycle-calibrated magnetostratigraphy of middle Carnian from South China: Implications for Late Triassic time scale and termination of the Yangtze Platform. *Palaeogeography, Palaeoclimatology, Palaeoecology 436*, 135–166. https://doi.org/10.1016/j.palaeo.2015.05.033

Zhang, Y., Ogg, J.G., Franz, M., Bachmann, G.H., Szurlies, M., Röhling, H.G., Li, M., Rolf, C. & Obst, K. 2020: Carnian (Late Triassic) magnetostratigraphy from the Germanic Basin allowing global correlation of the mid-Carnian episode. *Earth and Planetary Science Letters 541*. https://doi.org/10.1016/j.epsl.2020.116275

Section/polarity set	Mean Dec/Inc (°)	k (α_{95}[°])	$N_S/N_T/N_l/N_p$	Reversal Test [γ_o/γ_c] (°)	VGP Lat/Long (°)	Dp/Dm [paleolat.] (°)	A95 (min, max), $\%VGP_{45}$ (°)
Nørdstefjellet (N)	45.9/67.3	32.4(4.2)	15/66/20/17	-	-	-	-
Nørdstefjellet (R)	244.8/-73.8	15.6 (8.5)	13/66/0/21	-	-	-	-
Nørdstefjellet (all)	50.4/69.5	18.3 (3.0)	28/66/20/38	Rc, [9/12.5]^S	60.1/137.6	4.4/5.1 [53.2]	5.3 (3.2,10.1),1.5
Binnedalen(N)	47.5/68.9	47.5 (2.7)	28/94/40/18	-	-	-	-
Binnedalen (R)	232.6/-70.8	31.4 (5.5)	18/94/1/23	-	-	-	-
Binnedalen (all)	48.9/69.5	29.4 (2.0)	47/94/41/41	Rb [2.6/5.6]^C	60.5/139.3	3.0/3.5 [53.2]	4.8 (2.6, 7.3), 4.3
Hopen (all)	49.5/69.5	37.0 (1.7)	75/160/21/61	Rb [4.6/5.2]^C	60.3/138.6	2.5/2.9 [53.2]	3.5 (2.1, 5.4), 3.1
Tumlingodden (N)	35.2/60.9	39.3 (11.0)	4/49/3/3				-
Tumlingodden (R)	202.9/-71.0	25.2 (6.9)	14/49/3/14				-
Tumlingodden (all)	27.1/68.5	19.0 (4.5)	21/49/6/17	Rc [11.2/13.2]^C	61.0/163.8	6.4/7.6 [51.7]	10.0 (3.6, 12.1), 2.2

Table 1. Mean palaeomagnetic directions for the sections. Specimen set code, N=normal, R=reverse. k (α_{95}) = Fisher concentration parameter and 95% cone of confidence. N_S =number of sample levels (sites), N_T=Total specimens measured, N_l=Number of specimens with line-fits, N_p=Number of specimens with great circle (GC) fits. GC mean uses method of McFadden & McElhinney (1988) using N_l+N_p data, and Fisher mean N_l data. For the reversal test (McFadden & McElhinny, 1990), γ_o=observed angle; γ_c=critical angle, c=common-k test, s= simulation test. Virtual geomagnetic pole (VGP) is the normal pole. A95 (min, max) = Fisher 95% confidence interval for the site mean VGP direction (N_s sites), and $A95_{min}$ and $A95_{max}$ threshold values of Deenen et al. (2011, 2014). $\%VGP_{45}$= percent of samples yielding VGP latitude < |45°|, as a reflection of the match to the modern geomagnetic field and field models in which $\%VGP_{45}$ is 3-4% (Cromwell et al., 2018). Statistics determined with Pmagtool v.5 (Hounslow, 2006).

Figure 1. Location of the magnetostratigraphic sampling sites (marked in red) on (A) Eastern Svalbard at Tumlingodden on Wilhelmøya and (B), (C) at Nørdstefjellet and Binnedalen on Hopen. Geology maps from Mørk et al. (1999). Other sections and cores discussed in text on Spitsbergen also marked on Svalbard map in (B).

Figure 2. (A) Lithostratigraphy and sequence stratigraphy (2^{nd} and 3^{rd} order sequences) of central and eastern Svalbard and the Barents Sea region adjacent to the Carnian (from Mørk et al., 2013, Klausen et al., 2015; Lord et al., 2017). Intervals of hiatus in late Carnian and late Ladinian (in white) based on this work and Hounslow et al. (2008b) respectively. Base Norian based on this work. (B) Palynological zonations in the interval of the upper Storfjorden to lower Wilhelmøya subgroups (based on Paterson & Mangerud, 2015, 2020). A, a, c, r are: acme, abundant, common and rare first and last occurrences.

Figure 3. Correlation of the sedimentary log to the photograph of the cliff just north of the Binnedalen section. Interpretative correlated layers labelled (see text for details). Channel sandstone numbers (1 and 2) of Solvi (2013).

Figure 4. Correlation of the sedimentary log to the Nørdstefjellet section photograph. Interpretative correlated layers labelled (see text for details). Channel sandstone numbers (1 and 2) of Solvi (2013).

Figure 5. Log and sample location (sample codes WI) on the Tumlingodden section from Wilhelmøya. The magnetic polarity of the sample horizons are also shown. Placement of the base of the Isfjorden Member based on the Tumlingodden 10-1 log of Lord et al. (2017). Samples were placed on the sedimentary log of the section created by Rita Sande Rød.

Figure 6. Sample position on the Binnedalen and Nørdstefjellet logs, showing how the samples from the Nørdstefjellet section were projected onto the composite height scale and log at Binnedalen. Correlation lines shown in blue are the photo correlation layers shown in Figs. 3 & 4. Base of the Hopen Member show in black line. Polarity composite from Fig. 9. Palynological zonation at Binnedalen from Paterson & Mangerud (2015).

Figure 7. Example demagnetization data for specimens from: a) to c) Nørdstefjellet; d), e) Binnedalen, and f), g) Tumlingodden sections. Each shows a Zijderveld plot and a stereographic projection of the demagnetisation steps. g) also shows a typical intensity decay plot illustrating the dominating intensity of the Brunhes component. Stereographic projection plots in equal area, with filled symbols (unfilled) lower hemisphere (upper). a), c), d), e) have some lower demagnetization steps removed to make the plots clearer. γ_{95} is the confidence cone statistic of flood from Briden & Arthur (1981). a) Specimen HO2.1 (height -30.7 m) interpreted as revere polarity, great circle (GC) trend, class T1, with a GC plane fit from NRM to 80 mT. LT component NRM to 15 mT. b) Specimen HO29.6 (height 151.5 m) interpreted as reverse polarity, with a GC trend, class T2, and a GC plane fit from 25 mT to 280°C. No LT component. c) Specimen HO31.5 (height 156.2 m) interpreted as normal polarity ChRM line fit, class S2, from 15 mT to the origin; No LT component. D) Specimen

2H25.2 (height 75.6 m) interpreted as reverse polarity GC line fit, class T1, with a GC plane fit from 40 mT to the origin. LT component 130ºC to 40 mT. E) Specimen 2h20.2 (height 62.9 m) interpreted as normal polarity ChRM line fit, class S3, from 10–40 mT. No LT component. f) Specimen WI6.1 (height 67 m) interpreted as revere polarity ChRM line fit, class S1, from 10–50 mT; LT component NRM to 10 mT. g) Specimen WI21.1 (height 129.8 m) interpreted as normal polarity ChRM line fit, class S3, from 40 mT to the origin. LT component NRM to 10 mT.

Figure 8. Characteristic remanence (ChRM) extracted from the specimens for: a) Nørdstefjellet, b) Binnedalen and c) Tumlingodden sections. In each the S-class directions are shown on the left, and the poles to the great circles shown on the right (used to determine the combined mean, and the VGP latitude). The single great circle shown on the right is that which is orthogonal to the ChRM mean direction. The great circle poles form a girdle along this great circle, indicating they can independently be used to determine a mean direction of the not-fully resolved Triassic component in these specimens.

Figure 9. Summary magnetostratigraphic, organic carbon isotope ($\delta^{13}C_{org}$) and % carbon data from Hopen. Positions of possibly erosional hiatuses, and maximum flooding surface (MFS) are shown. Demagnetisation behaviour described in text. Specimen polarity is the interpreted polarity for all measured specimens, with R and N grades indicating high quality data, R?, R?? and N?, N?? lower quality and ? indicating no interpretation possible. VGP latitude is the latitude of the specimen VGP direction with respect to the section mean normal polarity palaeopole position, with positive values indicating normal polarity. Carbon isotope data and maximum flooding surface (MFS) from Paterson et al. (2016) is shown for the Binnedalen section in the De Geerdalen Formation, and Lyngefjellet section for the Flatsalen Formation.

Figure 10. Summary magnetostratigraphic data from the east Tumlingodden section. See Figure 9 for details.

Figure 11. (A) Organic carbon isotope data ($\delta^{13}C_{org}$) from this study vs. the percentage of organic carbon (%carbon). (B) Percentage carbon and total nitrogen (N_T) with the upper range of N_T (i.e., > c. 0.03%) indicating a colinear change with %carbon, indicating the same organic matter source and a lower range in which the nitrogen has a dominantly inorganic source. The y-axis intercept of the regression line provides an estimate of the average inorganic nitrogen (Goñi et al., 1998).

Figure 12. (A) Range of $\delta^{13}C_{org}$ in selected studies (y-axis scale as in b) of the Late Triassic, divided into terrestrial source and marine-sourced organic matter. The grey and green boxes indicate the approximate expected range of terrestrial and marine sources, respectively. Data are also shown from the early Carnian and late Ladinian of Spitsbergen from Mueller et al. (2016). (B) $\delta^{13}C_{org}$ and inorganic-nitrogen corrected C/N ratios of the Hopen samples laid over fields of typical ranges proposed by Meyers (1994), Twichell (2002) and Fang et al. (2013), indicating the Hopen samples generally fall into the terrestrial range of C/N. (C) Those sample in which inorganic-nitrogen corrected C/N ratios could not be determined, indicating that the CIEs in the Hopen sections are largely from samples with lower organic

carbon (same y-axis scale as in b).

Figure 13. Compilation of selected carbon isotope data in the late Carnian and across the Carnian–Norian boundary. (A) Silická Brezová from Korte et al. (2005), with relationship to magnetostratigraphy as in Mueller et al. (2016). Samples in red not used in the curve fit. (B) Qingyin Gou section data from Jin et al. (2019) and Zhang et al. (2015). (C) Pizzo Modello from Muttoni et al., (2004, 2014) and Mazza et al. (2010). Samples in red not used in the curve fit. (D) Black Bear Ridge organic carbon isotope ($\delta^{13}C_{org}$) data (black dots, red curve) from Williford et al. (2007b), and carbonate carbon ($\delta^{13}C_{carb}$) data from Onoue et al. (2016) and Lei et al. (2021). Unfilled red circles of Lei et al. (2021) not used in curve fit. The inferred negative carbon isotope excursions in the Tuvalian (TCIE) and Lacian (LCIE) are labelled sequentially from the base of the Tuvalian, with TCIE-1 equivalent to NCIE-3 of Dal Corso et al. (2018). b, md, wr = brachiopod, microdrilled and whole rock samples. Thick red correlation line is the base of the Norian correlated to Pizzo Mondello.

Figure 14. Comparison of the magnetostratigraphy from Hopen and Wilhelmøya with other key sections, with the inferred carbon isotope excursions marked in purple, and magnetostratigraphic correlations in red. Pignola-2 from Maron et al. (2017). Dalsnuten from Hounslow et al. (2007) and Mueller et al. (2016); Pizzo Mondello and Silická Brezová as in Fig. 13. Magnetochron labelling from Hounslow and Muttoni (2010), (H&M, 2010) with the revised Tuvalian polarity composite from this work, and Tuvalian-1 data from the Dalsnuten and Pignola-2 section data on the left.

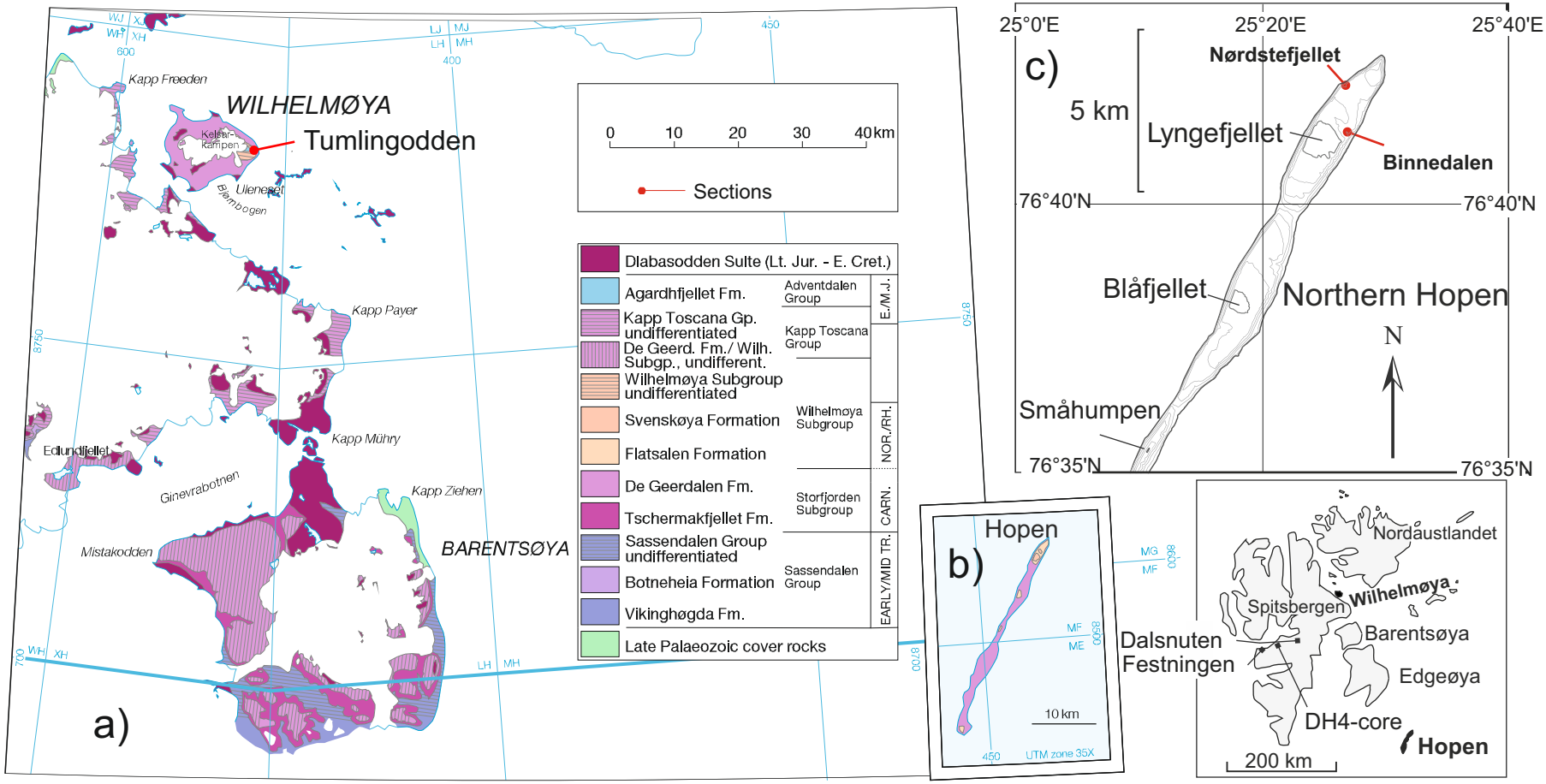
a)
WILHELMØYA
Tumlingodden
Kapp Freeden
Kapp Payer
Kapp Mühry
Kapp Ziehen
Edlundfjellet
Ginevrabotnen
Mistakodden
BARENTSØYA
Kelsar-kampen
Ulenesset
Bjørnbogen
0 10 20 30 40 km
Sections
Dlabasodden Sulte (Lt. Jur. - E. Cret.)
Agardhfjellet Fm.
Adventdalen Group
Kapp Toscana Gp. undifferentiated
De Geerd. Fm./ Wilh. Subgp., undifferent.
Kapp Toscana Group
Wilhelmøya Subgroup undifferentiated
Svenskøya Formation
Wilhelmøya Subgroup
Flatsalen Formation
De Geerdalen Fm.
Tschermakfjellet Fm.
Storfjorden Subgroup
Sassendalen Group undifferentiated
Botneheia Formation
Sassendalen Group
Vikinghøgda Fm.
Late Palaeozoic cover rocks
E./M.J.
NOR./RH.
CARN.
EARLY/MID TR.
b)
Hopen
10 km
UTM zone 35X
c)
5 km
Nørdstefjellet
Lyngefjellet
Binnedalen
Blåfjellet
Northern Hopen
N
Småhumpen
25°0'E
25°20'E
25°40'E
76°40'N
76°35'N
Nordaustlandet
Spitsbergen
Wilhelmøya
Barentsøya
Edgeøya
Dalsnuten
Festningen
DH4-core
Hopen
200 km

Fig. 1.

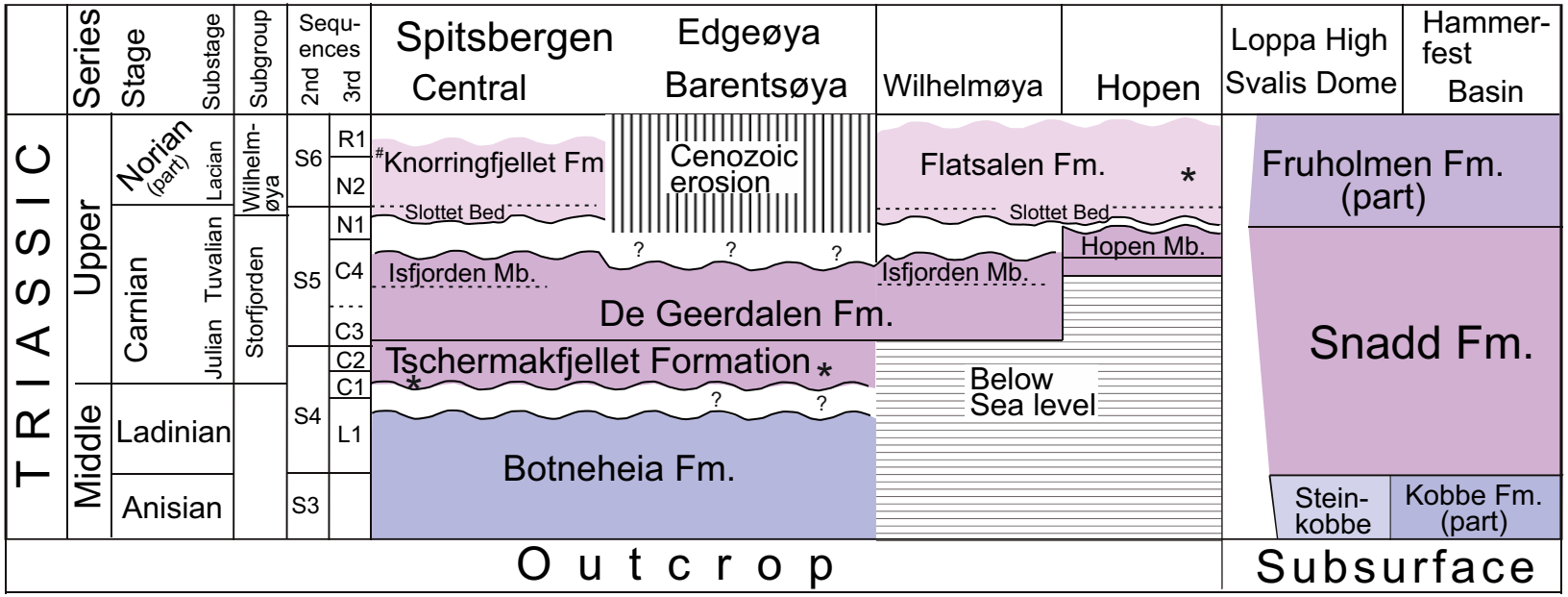

* ammonoid bearing levels in Upper Triassic, # lowest part only

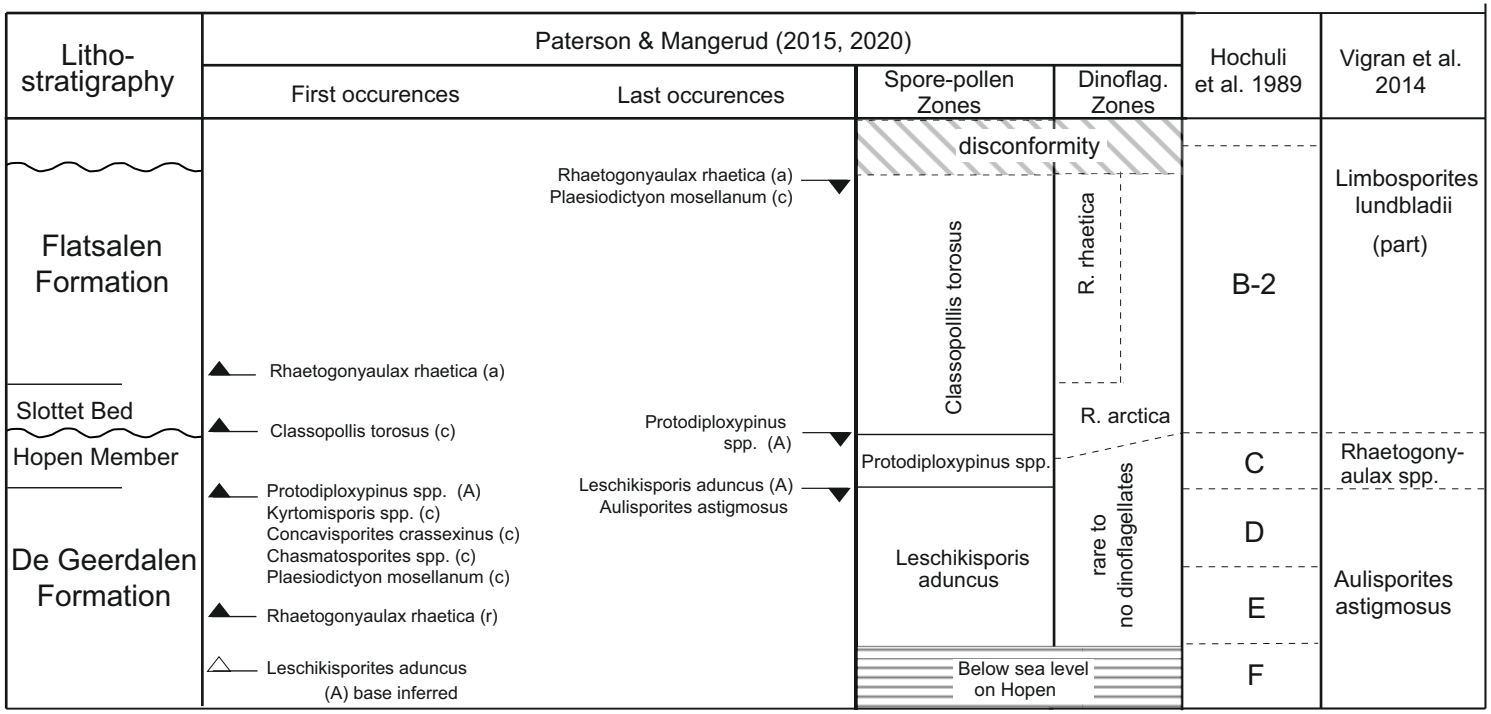

Fig. 2.

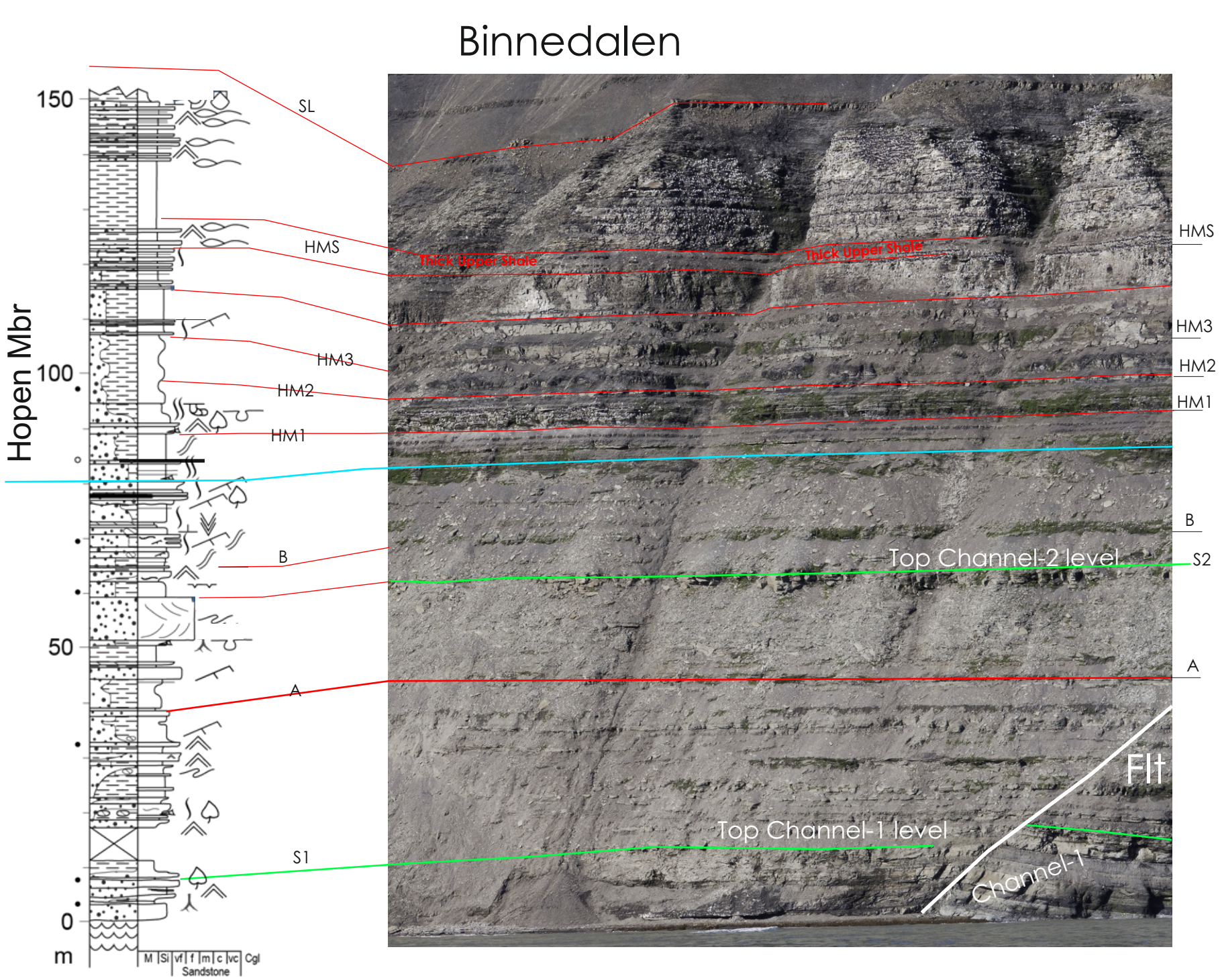
Binnedalen
Hopen Mbr
150
100
50
0
m
SL
HMS
HM3
HM2
HM1
B
A
S1
M
Si
vf
f
m
c
vc
Cgl
Sandstone
Thick Upper Shale
Thick Upper Shale
HMS
HM3
HM2
HM1
B
S2
Top Channel-2 level
A
Flt
Top Channel-1 level
Channel-1

Fig. 3.

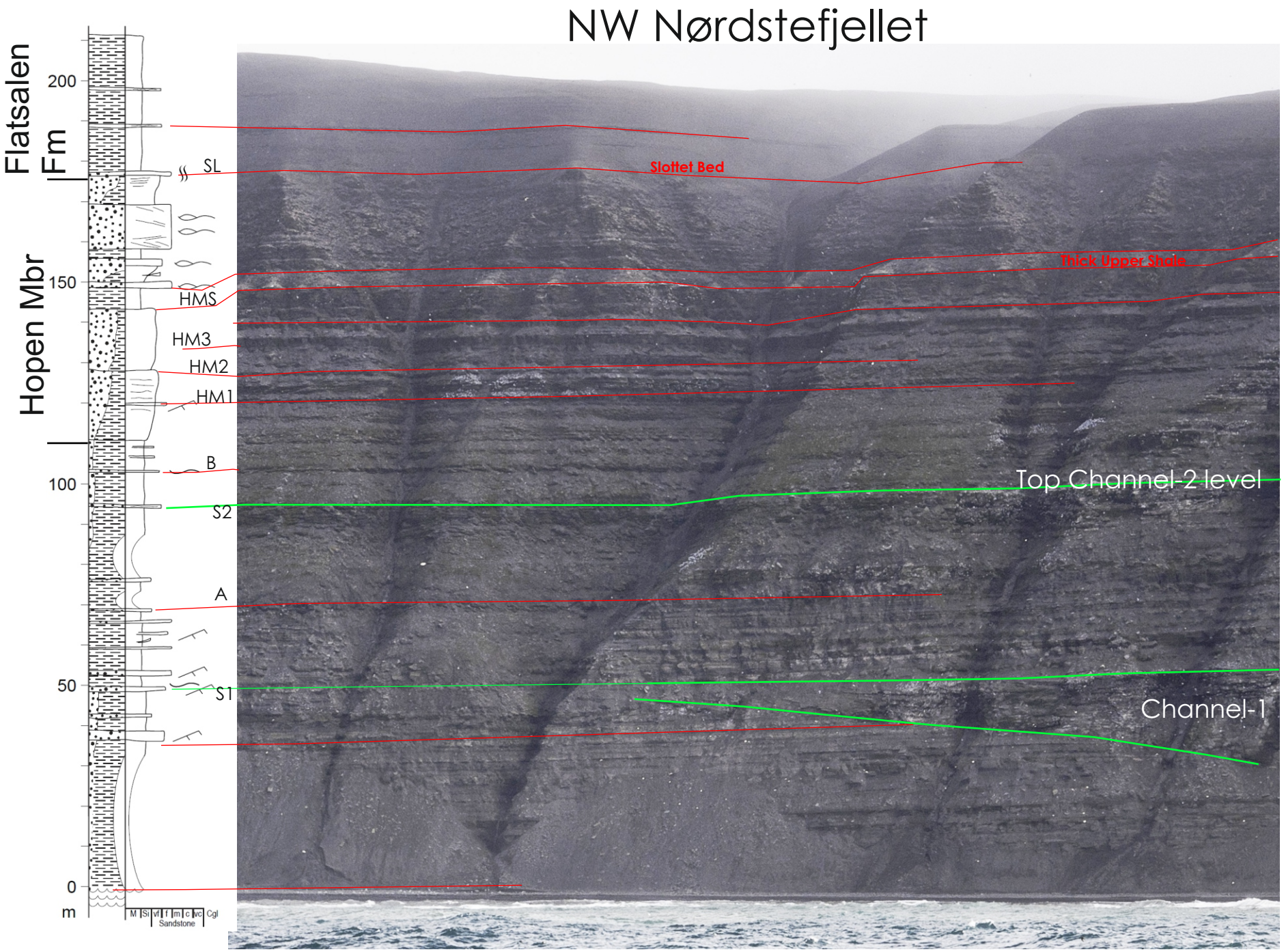
NW Nørdstefjellet
Flatsalen Fm
Hopen Mbr
200
150
100
50
0
m
SL
HMS
HM3
HM2
HM1
B
S2
A
S1
M Si Vf f m c Vc Cgl
Sandstone
Slottet Bed
Thick Upper Shale
Top Channel-2 level
Channel-1

Fig. 4.

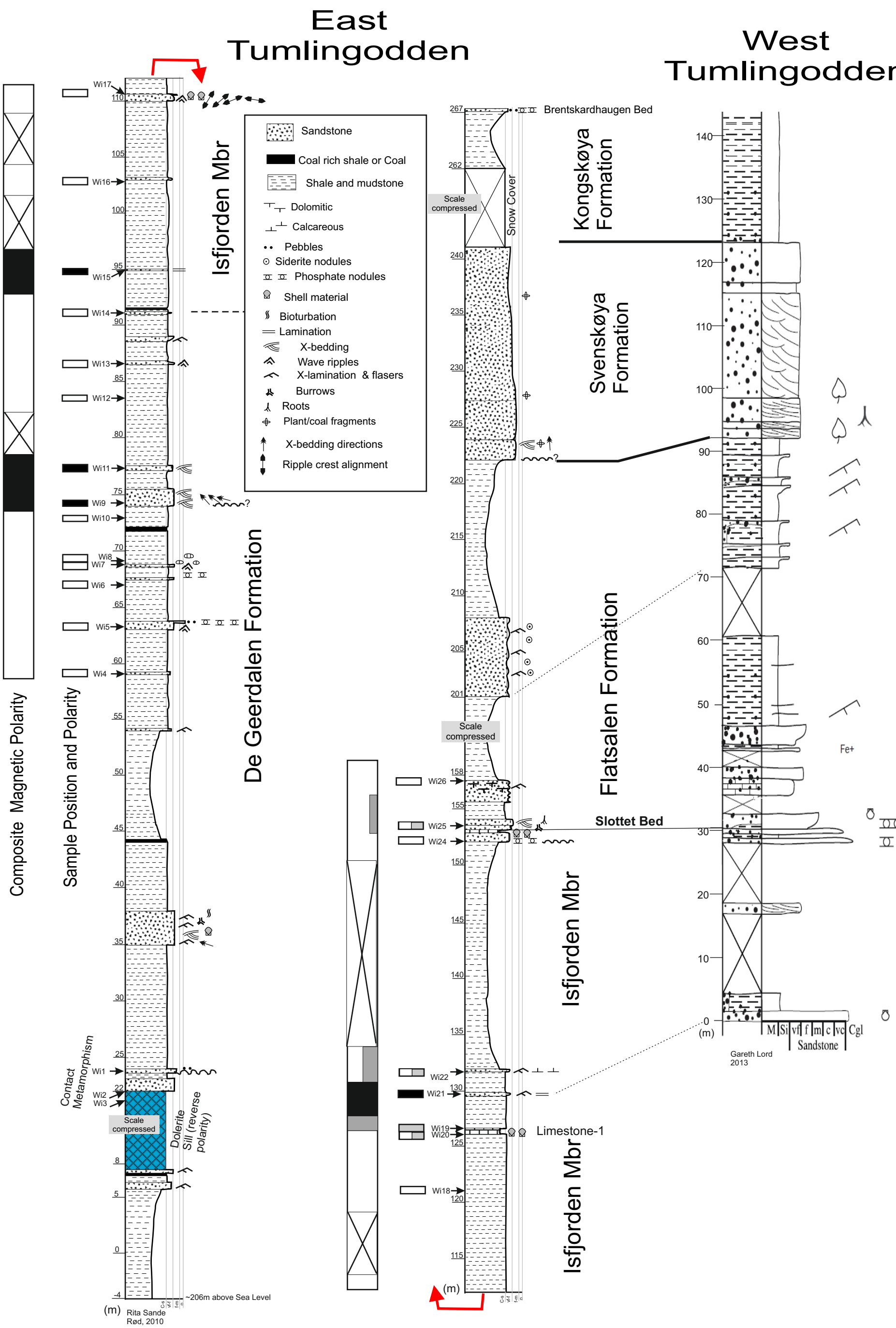
East Tumlingodden
West Tumlingodden
Composite Magnetic Polarity
Sample Position and Polarity
Isfjorden Mbr
De Geerdalen Formation
Flatsalen Formation
Svenskøya Formation
Kongskøya Formation
Brentskardhaugen Bed
Snow Cover
Scale compressed
Slottet Bed
Limestone-1
Contact Metamorphism
Dolerite Sill (reverse polarity)
~206m above Sea Level
Rita Sande Rød, 2010
Gareth Lord 2013
Sandstone
Coal rich shale or Coal
Shale and mudstone
Dolomitic
Calcareous
Pebbles
Siderite nodules
Phosphate nodules
Shell material
Bioturbation
Lamination
X-bedding
Wave ripples
X-lamination & flasers
Burrows
Roots
Plant/coal fragments
X-bedding directions
Ripple crest alignment
Wi1
Wi2
Wi3
Wi4
Wi5
Wi6
Wi7
Wi8
Wi9
Wi10
Wi11
Wi12
Wi13
Wi14
Wi15
Wi16
Wi17
Wi18
Wi19
Wi20
Wi21
Wi22
Wi24
Wi25
Wi26
(m)

Fig. 5.

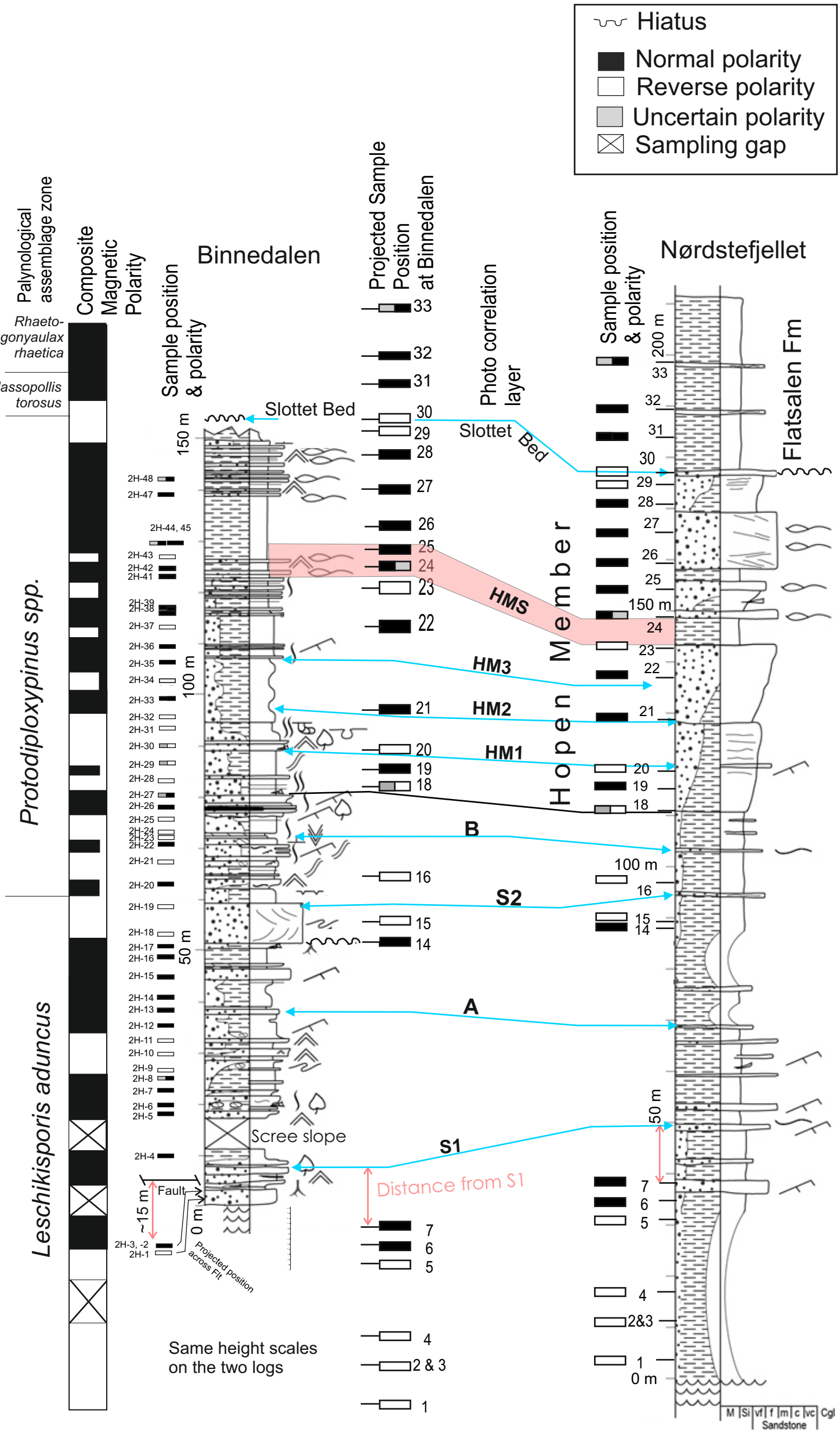
Hiatus
Normal polarity
Reverse polarity
Uncertain polarity
Sampling gap
Palynological assemblage zone
Composite Magnetic Polarity
Rhaeto-gonyaulax rhaetica
Classopollis torosus
Protodiploxypinus spp.
Leschikisporis aduncus
Binnedalen
Sample position & polarity
Projected Sample Position at Binnedalen
Photo correlation layer
Slottet Bed
150 m
100 m
50 m
2H-48
2H-47
2H-44, 45
2H-43
2H-42
2H-41
2H-39
2H-38
2H-37
2H-36
2H-35
2H-34
2H-33
2H-32
2H-31
2H-30
2H-29
2H-28
2H-27
2H-26
2H-25
2H-24
2H-23
2H-22
2H-21
2H-20
2H-19
2H-18
2H-17
2H-16
2H-15
2H-14
2H-13
2H-12
2H-11
2H-10
2H-9
2H-8
2H-7
2H-6
2H-5
2H-4
2H-3, -2
2H-1
33
32
31
30
29
28
27
26
25
24
23
22
21
20
19
18
16
15
14
7
6
5
4
2 & 3
1
HMS
HM3
HM2
HM1
B
S2
A
S1
Fault
~15 m
0 m
Scree slope
Projected position across Flt
Distance from S1
Same height scales on the two logs
Nørdstefjellet
Sample position & polarity
Hopen Member
Flatsalen Fm
200 m
150 m
100 m
50 m
0 m
33
32
31
30
29
28
27
26
25
24
23
22
21
20
19
18
16
15
14
7
6
5
4
2&3
1
M Si vf f m c vc Cgl
Sandstone

Fig.6.

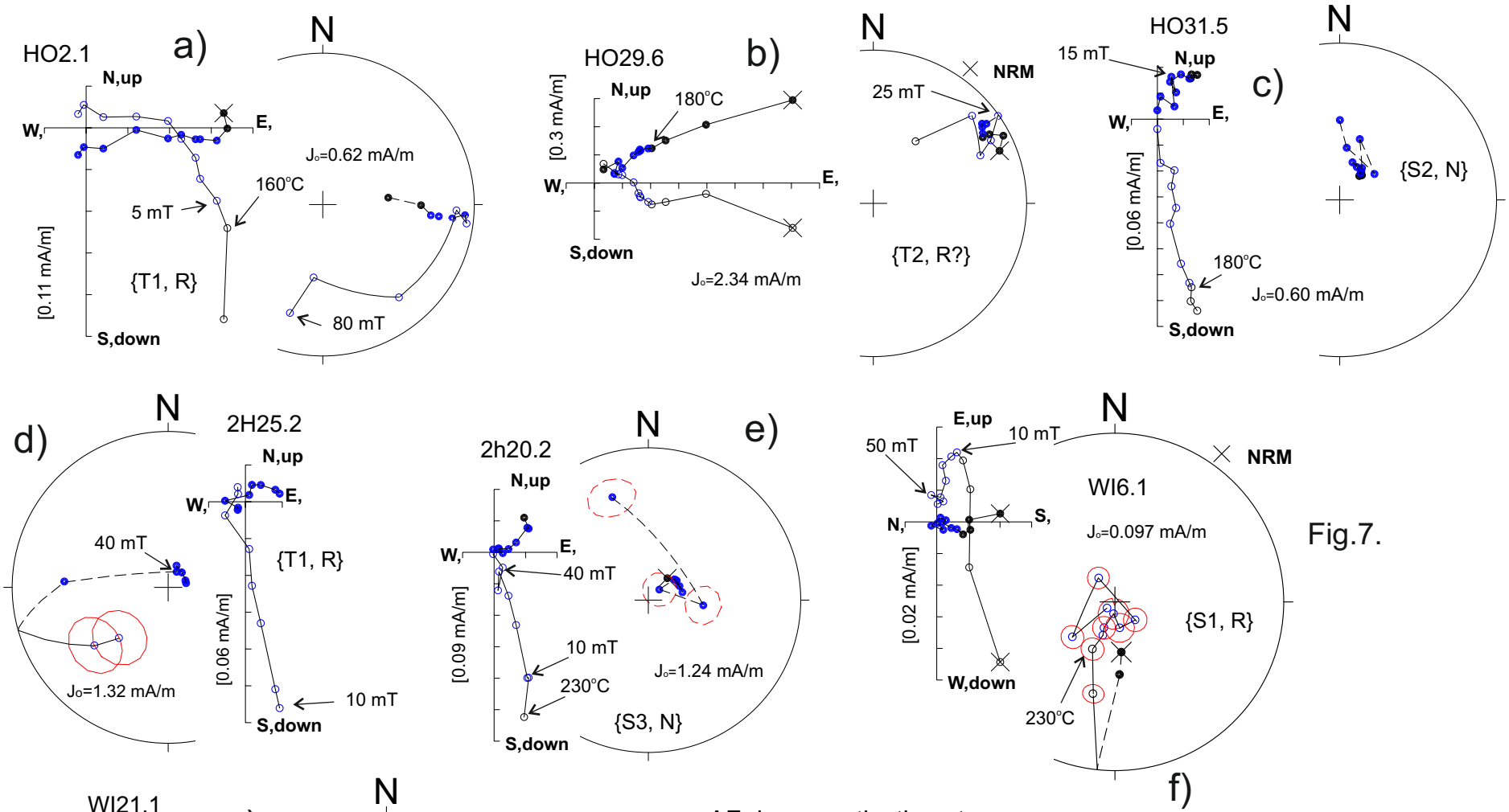

Fig.7.

- ● ○ AF demagnetisation steps
- ● ○ Thermal demagnetisation steps

Jo= NRM intensity

○ γ_{95} confidence cone (if > 4°)

● ○ Horizontal and vertical projections respectively (Zijderveld)

[..] = Zijderveld tick scale

{..} = Demagnetisation and polarity classification

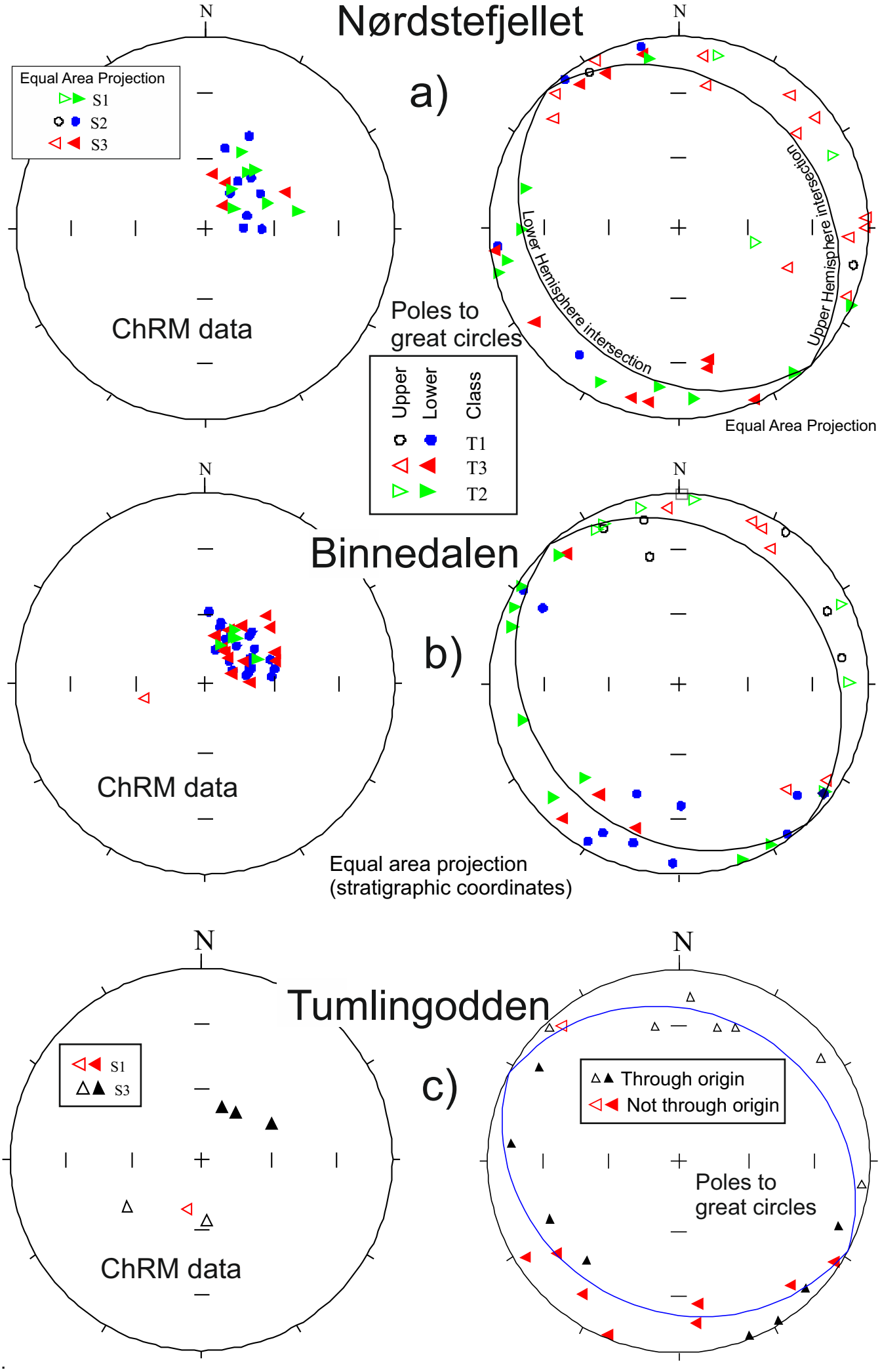
Nørdstefjellet
a)
N
Equal Area Projection
S1
S2
S3
ChRM data
Poles to great circles
Upper
Lower
Class
T1
T3
T2
Lower Hemisphere intersection
Upper Hemisphere intersection
Equal Area Projection
Binnedalen
b)
ChRM data
Equal area projection
(stratigraphic coordinates)
Tumlingodden
c)
S1
S3
ChRM data
Through origin
Not through origin
Poles to great circles

Fig. 8.

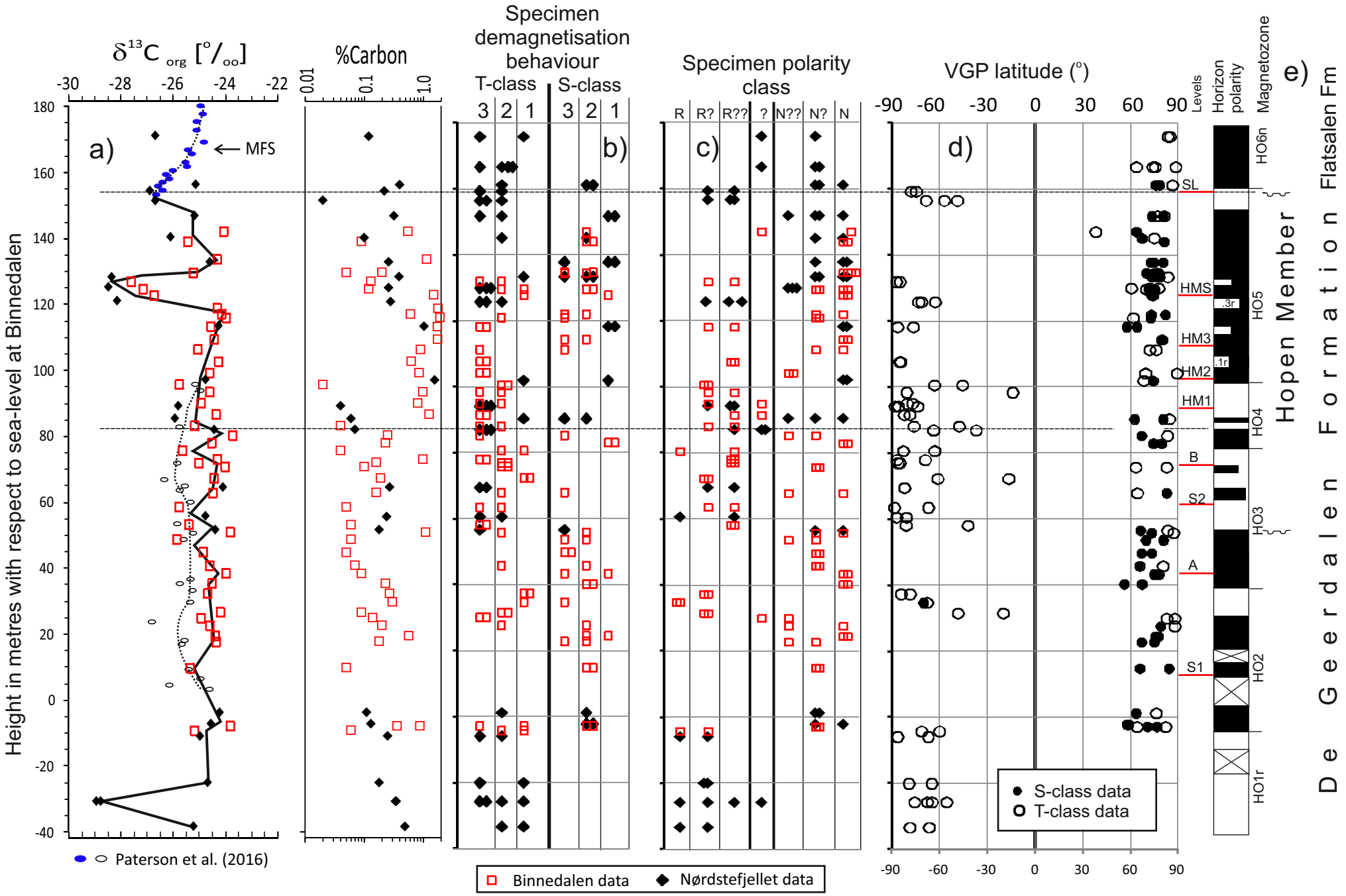
δ13C org [°/oo]
%Carbon
Specimen demagnetisation behaviour
T-class
S-class
Specimen polarity class
VGP latitude (°)
Levels
Horizon polarity
Magnetozone
Height in metres with respect to sea-level at Binnedalen
a)
b)
c)
d)
e)
MFS
Paterson et al. (2016)
Binnedalen data
Nørdstefjellet data
S-class data
T-class data
SL
HMS
HM3
HM2
HM1
B
S2
A
S1
HO6n
HO5
HO4
HO3
HO2
HO1r
Hopen Member
De Geerdalen Formation
Flatsalen Fm

Fig. 9.

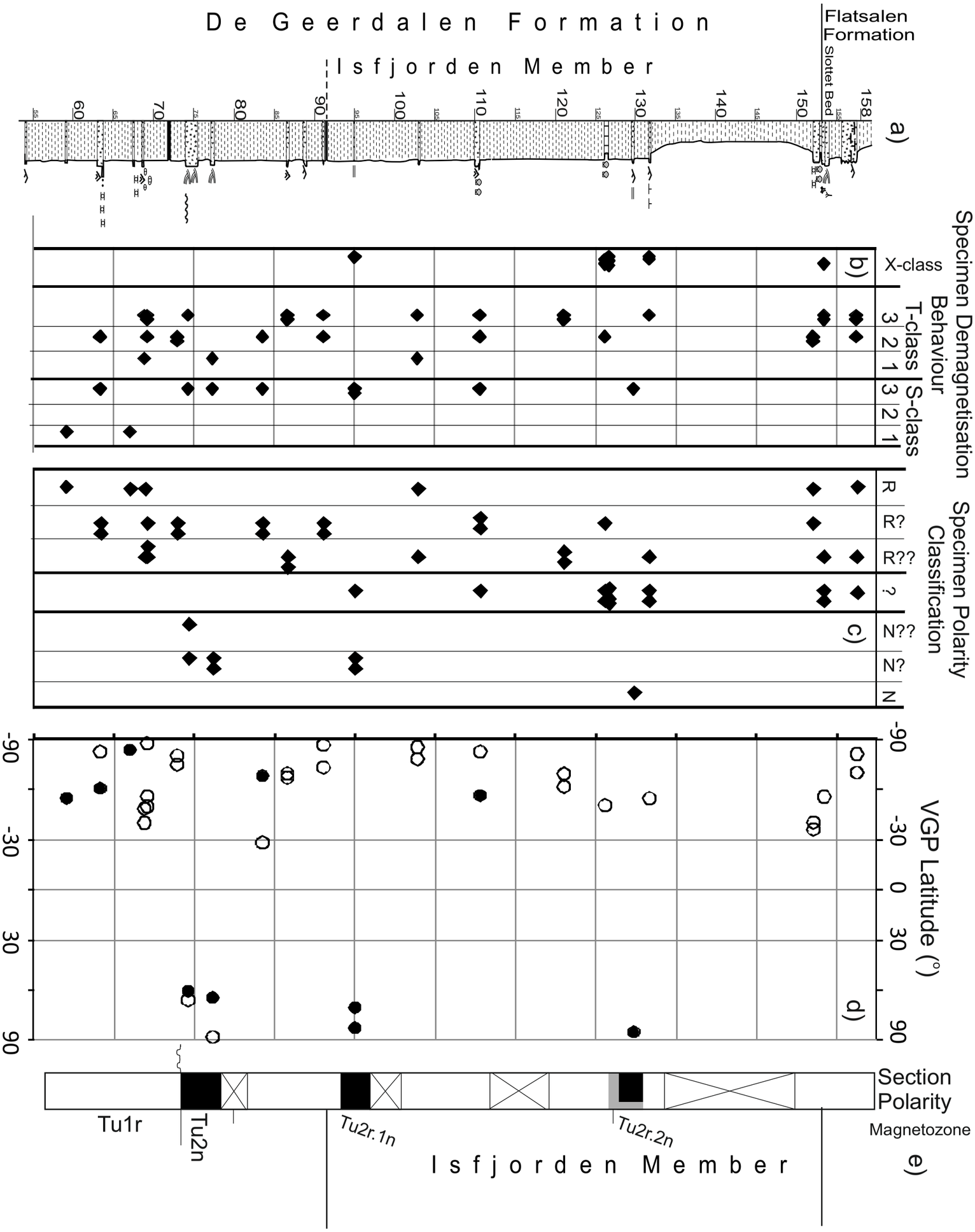
De Geerdalen Formation
Isfjorden Member
Flatsalen Formation
Slottet Bed
a)
b)
X-class
T-class
S-class
Behaviour
Specimen Demagnetisation
c)
Specimen Polarity Classification
R
R?
R??
?
N??
N?
N
d)
VGP Latitude (°)
-90
-30
0
30
90
e)
Section Polarity
Magnetozone
Tu1r
Tu2n
Tu2r.1n
Tu2r.2n
Isfjorden Member

Fig. 10.

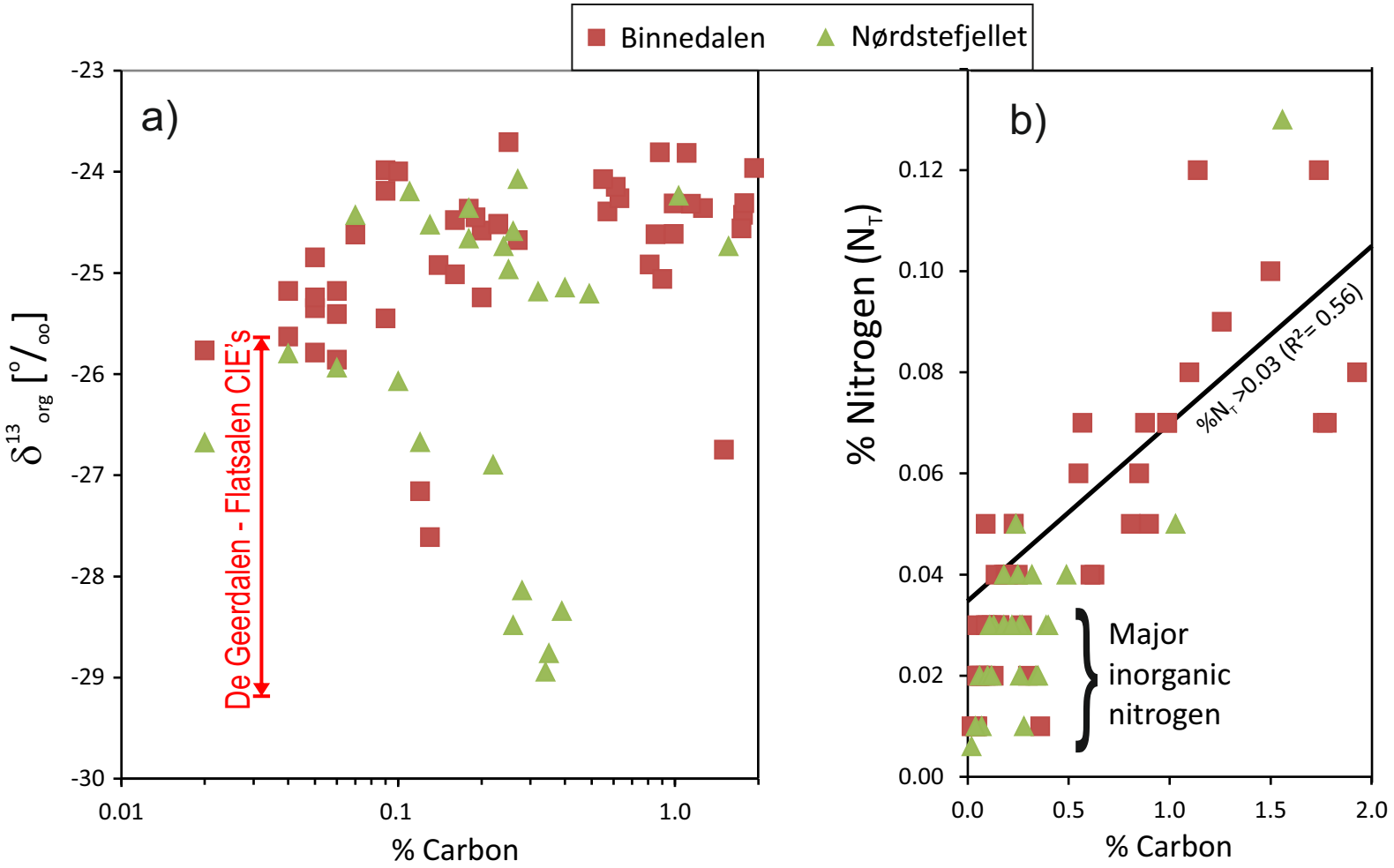
Binnedalen
Nørdstefjellet
a)
b)
-23
-24
-25
-26
-27
-28
-29
-30
0.01
0.1
1.0
% Carbon
δ13org [o/oo]
De Geerdalen - Flatsalen CIE's
0.12
0.10
0.08
0.06
0.04
0.02
0.00
0.0
0.5
1.0
1.5
2.0
% Nitrogen (NT)
%NT >0.03 (R2= 0.56)
Major
inorganic
nitrogen

Fig. 11.

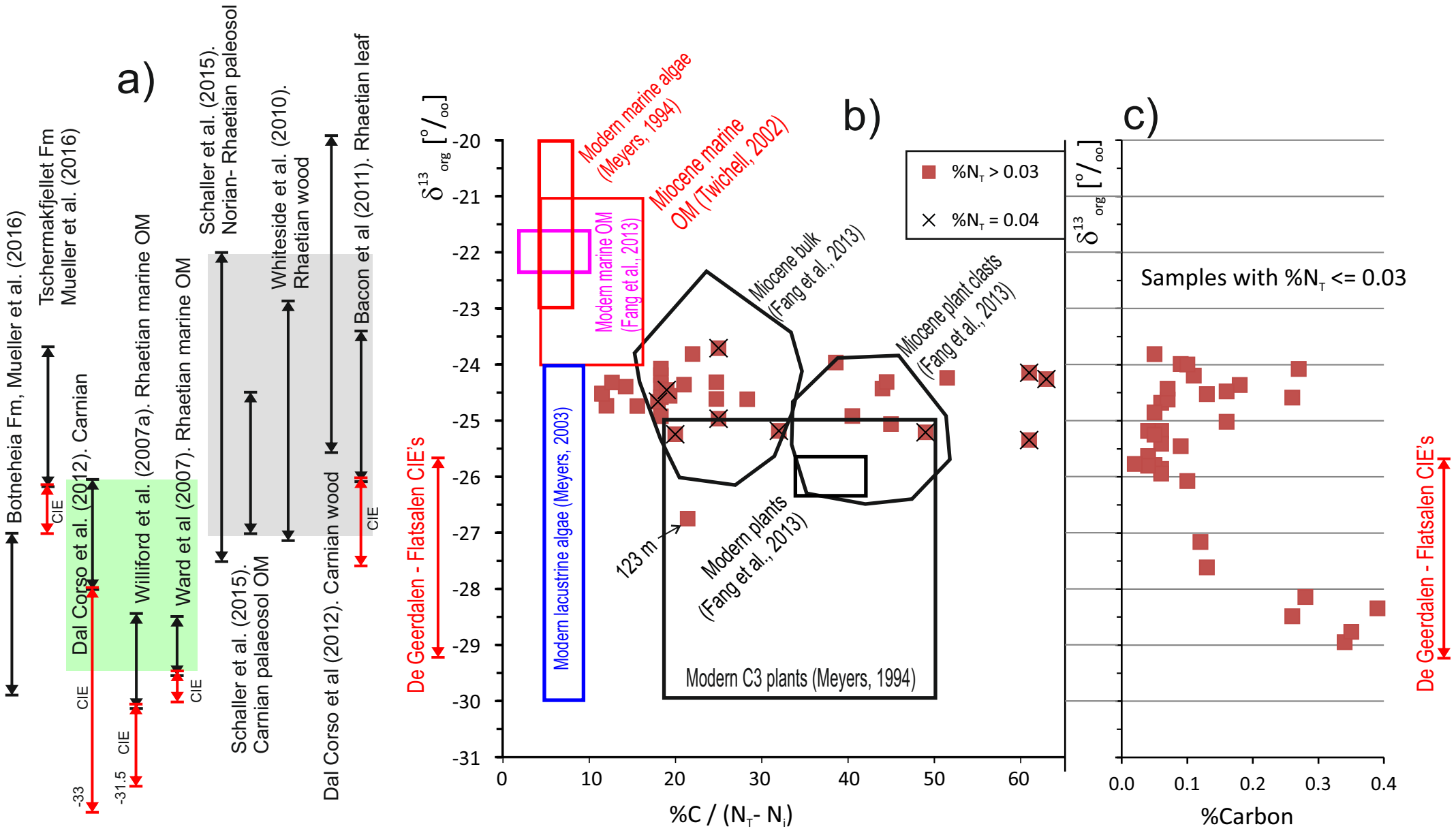
a)
Botneheia Fm, Mueller et al. (2016)
Tschermakfjellet Fm
Mueller et al. (2016)
Dal Corso et al. (2012). Carnian
Williford et al. (2007a). Rhaetian marine OM
Ward et al (2007). Rhaetian marine OM
Schaller et al. (2015).
Norian- Rhaetian paleosol
Whiteside et al. (2010).
Rhaetian wood
Bacon et al (2011). Rhaetian leaf
Schaller et al. (2015).
Carnian palaeosol OM
Dal Corso et al (2012). Carnian wood
CIE
-33
-31.5
b)
δ^{13}_{org} [°/oo]
-20
-21
-22
-23
-24
-25
-26
-27
-28
-29
-30
-31
Modern marine algae
(Meyers, 1994)
Miocene marine
OM (Twichell, 2002)
Modern marine OM
(Fang et al., 2013)
Miocene bulk
(Fang et al., 2013)
Miocene plant clasts
(Fang et al., 2013)
%N_T > 0.03
%N_T = 0.04
Modern lacustrine algae (Meyers, 2003)
123 m
Modern plants
(Fang et al., 2013)
Modern C3 plants (Meyers, 1994)
De Geerdalen - Flatsalen CIE's
0
10
20
30
40
50
60
%C / (N_T- N_i)
c)
δ^{13}_{org} [°/oo]
Samples with %N_T <= 0.03
0.0
0.1
0.2
0.3
0.4
%Carbon
De Geerdalen - Flatsalen CIE's

Fig. 12.

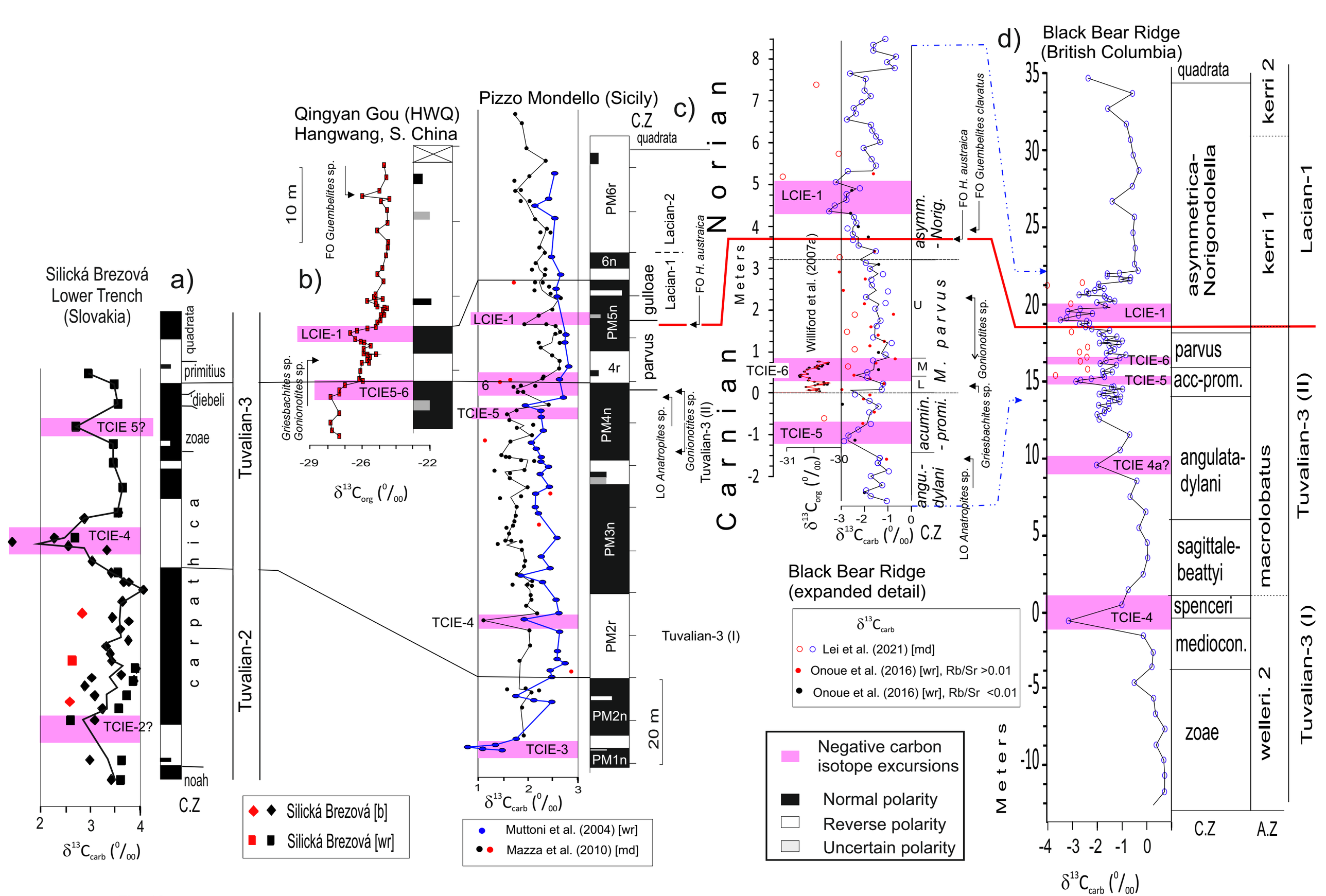
Silická Brezová
Lower Trench
(Slovakia)
a)
TCIE 5?
TCIE-4
TCIE-2?
quadrata
primitius
diebeli
zoae
a
c a r p a t h i c a
noah
C.Z
Tuvalian-3
Tuvalian-2
2
3
4
δ13Ccarb (0/00)
Silická Brezová [b]
Silická Brezová [wr]
Qingyan Gou (HWQ)
Hangwang, S. China
b)
10 m
FO Guembelites sp.
LCIE-1
TCIE5-6
Griesbachites sp.
Gonionotites sp.
-29
-26
-22
δ13Corg (0/00)
Pizzo Mondello (Sicily)
C.Z
c)
LCIE-1
6
TCIE-5
TCIE-4
TCIE-3
PM6r
6n
PM5n
4r
PM4n
PM3n
PM2r
PM2n
PM1n
20 m
quadrata
Lacian-2
Lacian-1
gulloae
parvus
LO Anatropites sp.
Gonionotites sp.
Tuvalian-3 (II)
Tuvalian-3 (I)
1
2
3
δ13Ccarb (0/00)
Muttoni et al. (2004) [wr]
Mazza et al. (2010) [md]
N o r i a n
C a r n i a n
Meters
8
7
6
5
4
3
2
1
0
-1
-2
LCIE-1
TCIE-6
TCIE-5
Williford et al. (2007a)
-31
-30
δ13Corg (0/00)
asymm. - Norig.
M. p a r v u s
acumin. - promi.
angu.- dylani
FO H. australica
FO Guembelites clavatus
Griesbachites sp.
Gonionotites sp.
LO Anatropites sp.
-3
-2
-1
0
δ13Ccarb (0/00) C.Z
Black Bear Ridge
(expanded detail)
δ13Ccarb
Lei et al. (2021) [md]
Onoue et al. (2016) [wr], Rb/Sr >0.01
Onoue et al. (2016) [wr], Rb/Sr <0.01
Negative carbon isotope excursions
Normal polarity
Reverse polarity
Uncertain polarity
d)
Black Bear Ridge
(British Columbia)
35
30
25
20
15
10
5
0
-5
-10
Meters
LCIE-1
TCIE-6
TCIE-5
TCIE 4a?
TCIE-4
quadrata
asymmetrica-
Norigondolella
parvus
acc-prom.
angulata-
dylani
sagittale-
beattyi
spenceri
mediocon.
zoae
kerri 2
kerri 1
welleri. 2
Lacian-1
macrolobatus
Tuvalian-3 (II)
Tuvalian-3 (I)
C.Z
A.Z
-4
-3
-2
-1
0
δ13Ccarb (0/00)

Fig. 13.

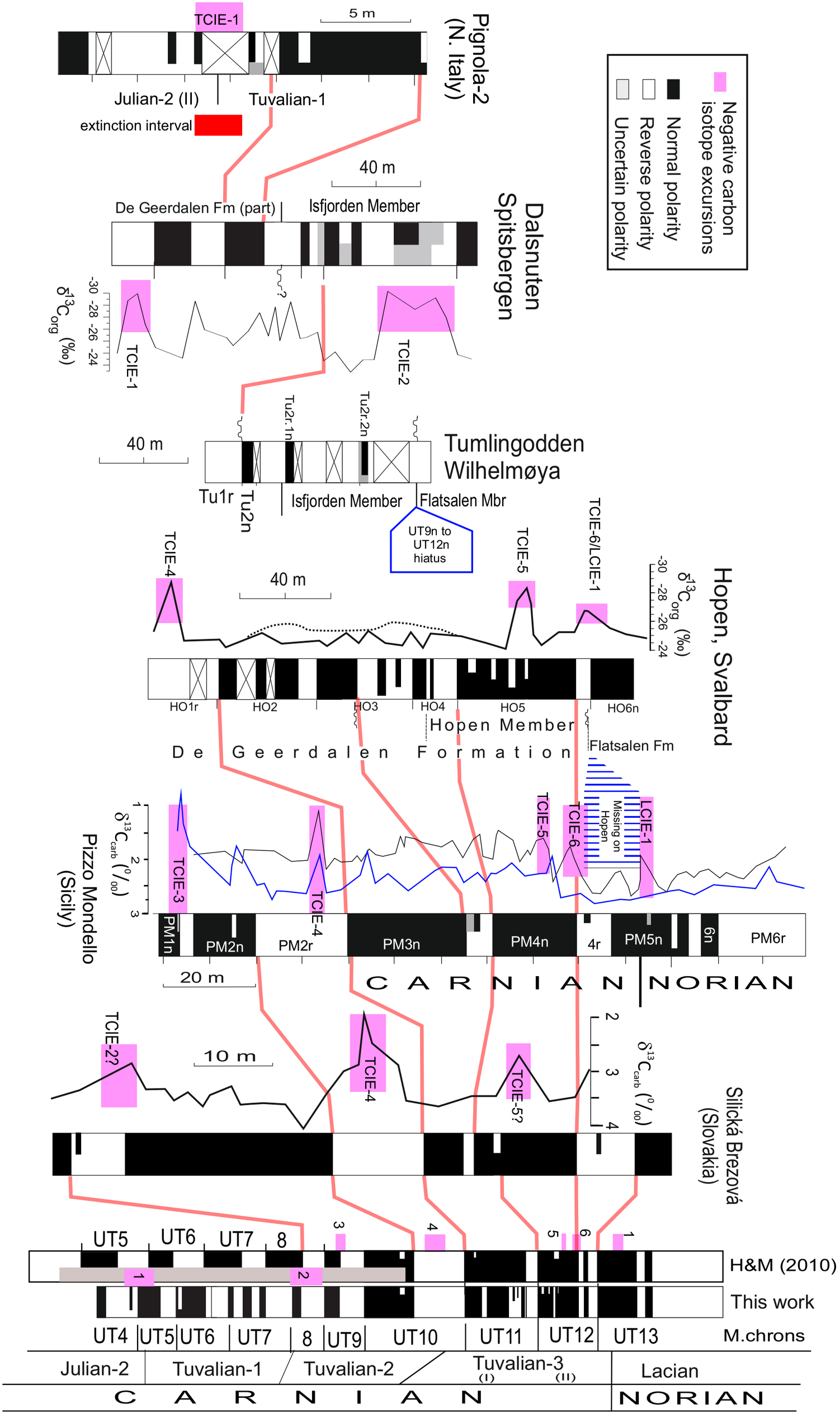
Negative carbon isotope excursions
Normal polarity
Reverse polarity
Uncertain polarity
Pignola-2 (N. Italy)
TCIE-1
5 m
Julian-2 (II)
Tuvalian-1
extinction interval
Dalsnuten Spitsbergen
40 m
De Geerdalen Fm (part)
Isfjorden Member
δ13Corg (‰)
-30 -28 -26 -24
TCIE-1
TCIE-2
Tumlingodden Wilhelmøya
Tu2r.1n
Tu2r.2n
40 m
Tu1r
Tu2n
Isfjorden Member
Flatsalen Mbr
UT9n to UT12n hiatus
Hopen, Svalbard
TCIE-4
TCIE-5
TCIE-6/LCIE-1
40 m
HO1r
HO2
HO3
HO4
HO5
HO6n
Hopen Member
De Geerdalen Formation
Flatsalen Fm
Missing on Hopen
LCIE-1
TCIE-6
TCIE-5
TCIE-4
TCIE-3
δ13Ccarb (‰)
Pizzo Mondello (Sicily)
PM1n
PM2n
PM2r
PM3n
PM4n
4r
PM5n
6n
PM6r
20 m
CARNIAN
NORIAN
TCIE-2?
10 m
TCIE-4
TCIE-5?
Silická Brezová (Slovakia)
UT5
UT6
UT7
8
1
2
3
4
5
6
H&M (2010)
This work
UT4
UT5
UT6
UT7
8
UT9
UT10
UT11
UT12
UT13
M.chrons
Julian-2
Tuvalian-1
Tuvalian-2
Tuvalian-3
(I)
(II)
Lacian
CARNIAN
NORIAN

Fig. 14.

Supplementary Information for: Geomagnetic polarity and carbon isotopic stratigraphic assessment of the late Carnian -earliest Norian in Svalbard: evidence for a major hiatus and improved Boreal to Tethyan correlation.

Mark W Hounslow, Samuel E Harris, Vassil Karloukovski & Atle Mørk

This supplementary information contains the following:

1) Additional section correlations and photographs (Fig. S1, S2)
2) Stereographic projections of the low stability component and the dolerite intrusion data (Fig. S3a, and S3b)
3) Down-section plots of the magnetic susceptibility (K) and NRM intensity (Figs S4, S5)
4) Data for thermal demagnetisation of a 3-axis IRM for four specimens (Fig. S6), and rock magnetic data for typical specimens from Binnedalen and Tumlingodden (Fig. S7; Table S1)
5) Discussion of the of the K- NRM intensity relationships for the De Geerdalen Formation and its adjacent units (Fig. S8).
6) Statistics of the line and great circle plane fits with respect to section, and demagnetisation class (Table S2).
7) Carbon isotope data (Table S3)
8) Compilation of the palaeomagnetic data for each specimen from all sections (in the associated excel file).

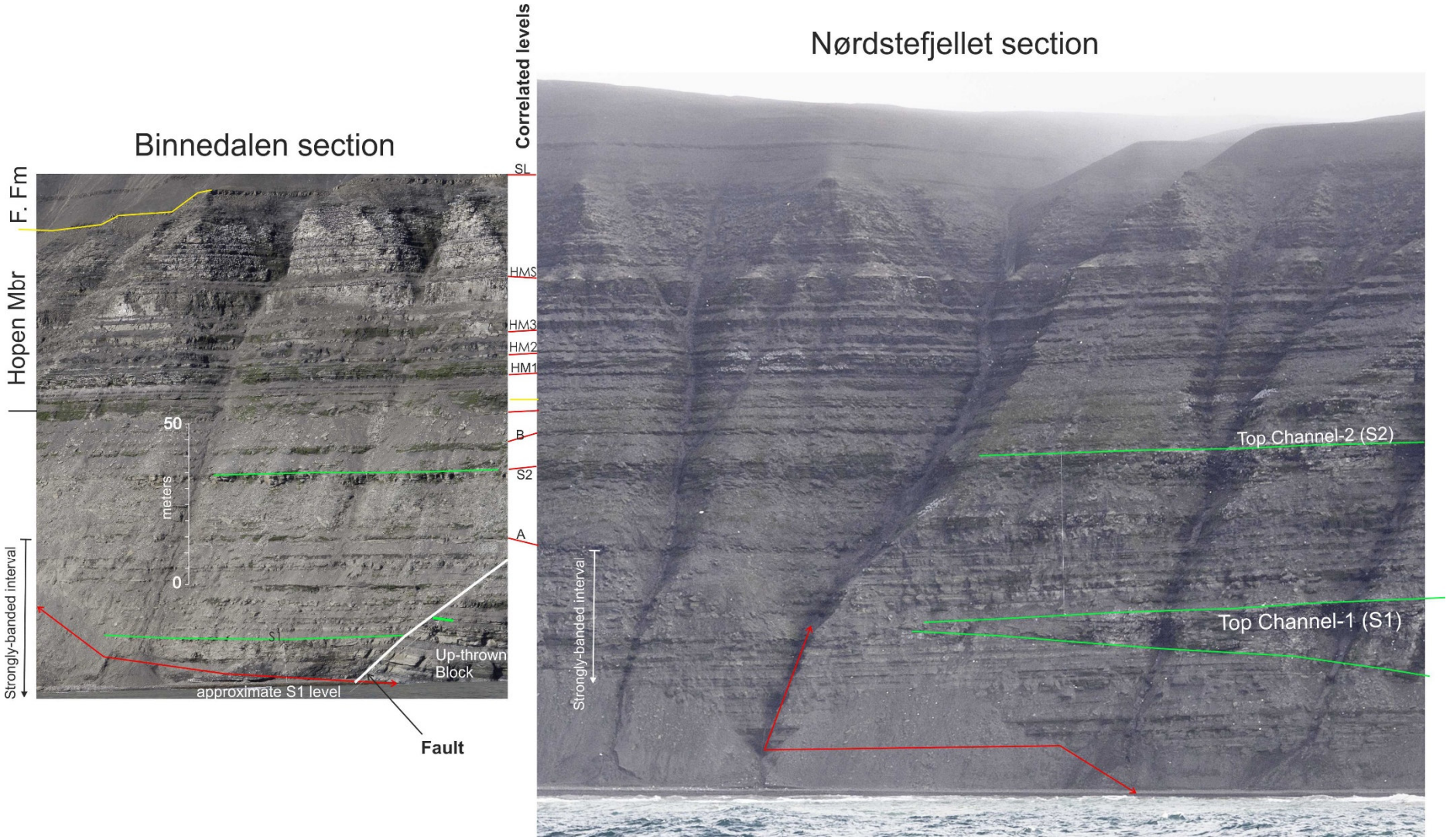

Fig. S1. Correlation of layers between the two sampled sections. The track of the sampled section is shown in red. Only the lower part of the Binnedalen section is shown, the main part of the section is to the left of the photo.

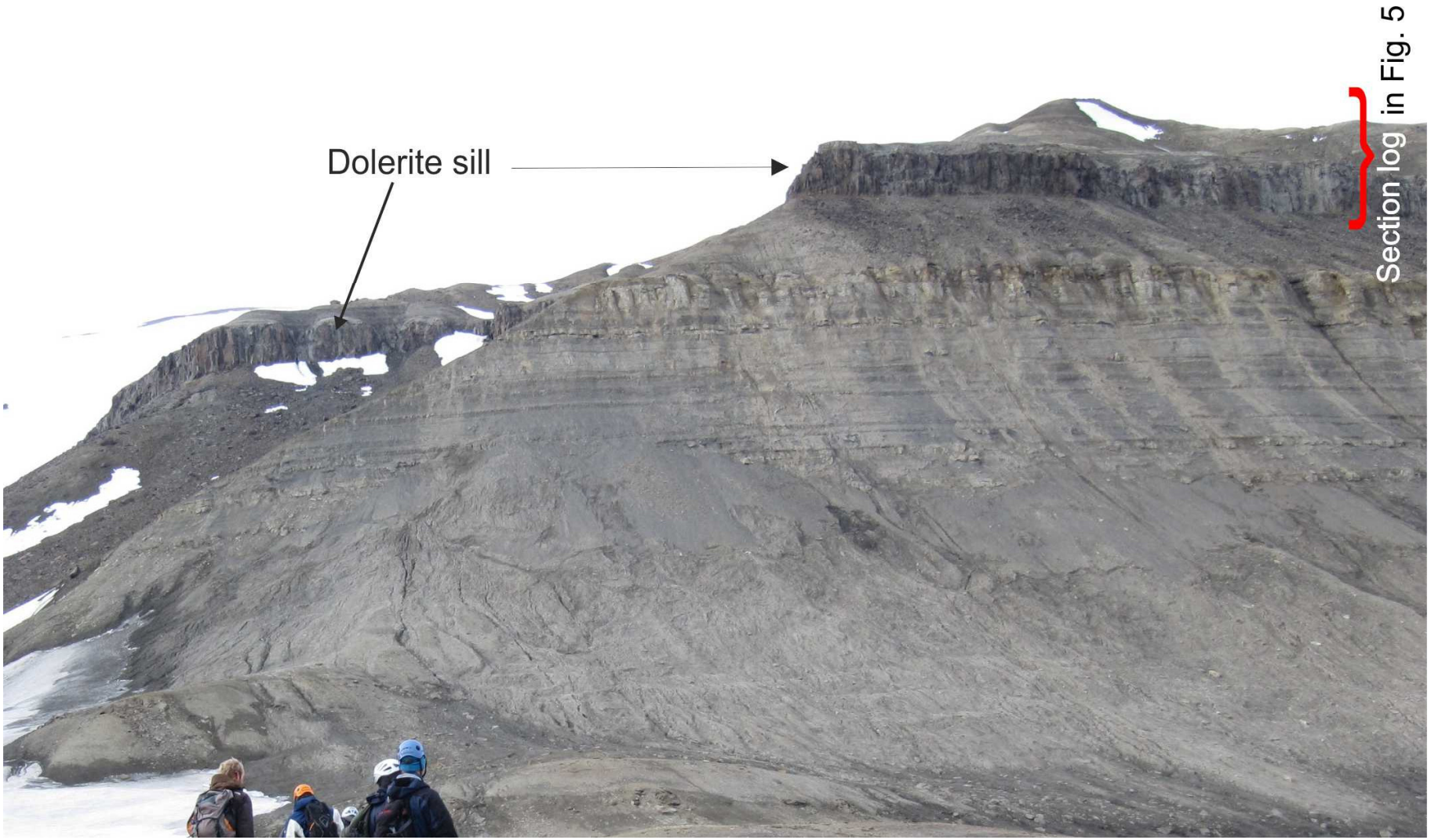

Fig. S2. The lower part of the Tumlingodden section. Sampling for this work started in the section above the dolerite sill, approximately in the mid De Geerdalen Fm. Here there is around 160 m of the De Deerdalen Formation from the base of slope to the dolerite sill (see Johansen, 2016, fig 8.2)

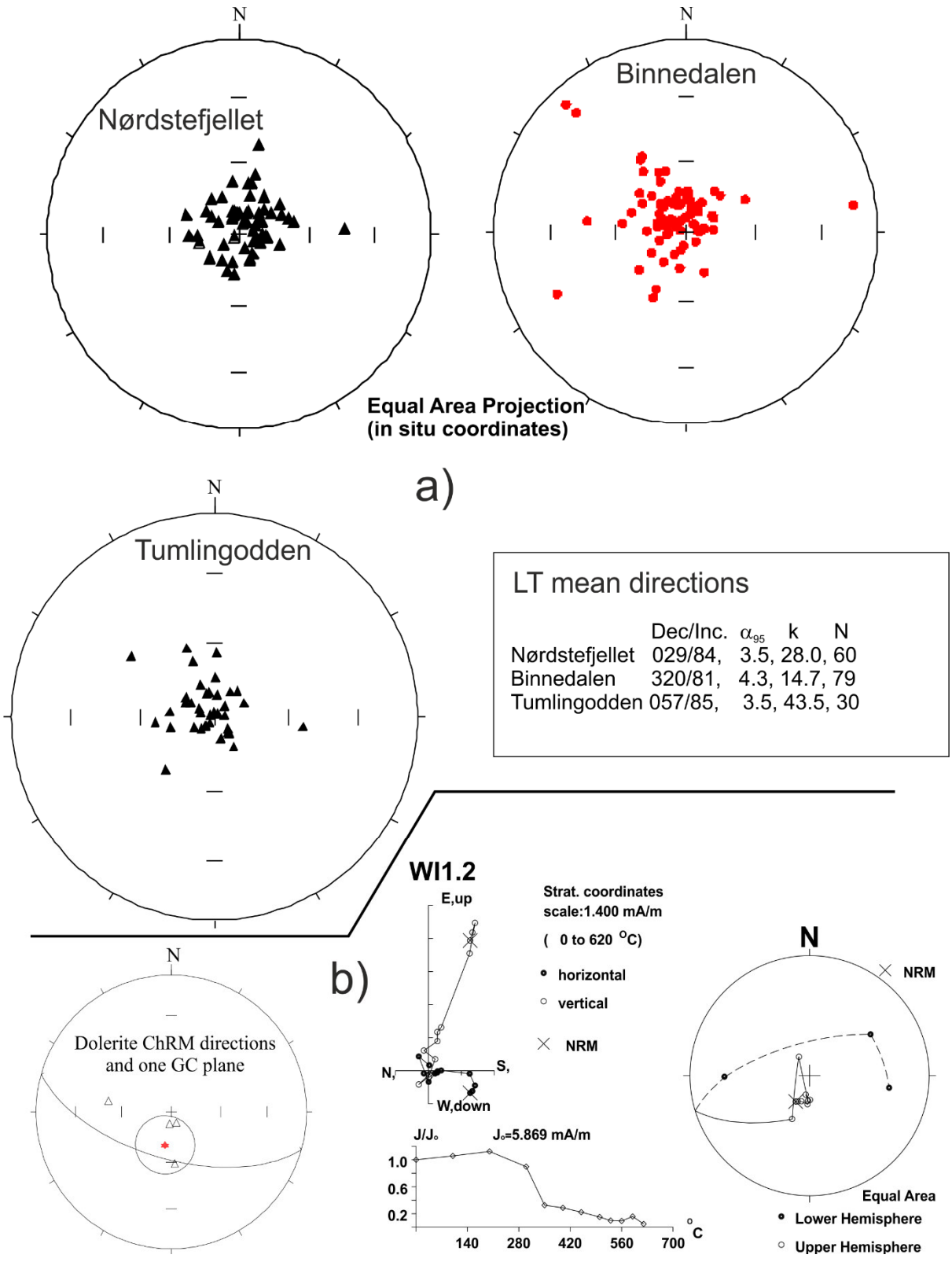

Fig. S3. A) Directional data from the low stability components. Data is in geographic coordinates. B) The ChRM directions of the dolerite intrusion in the Tumlingodden section, and it ChRM directional mean (also using the one great circle data, upper hemisphere projection of plane shown), along with example thermal demagnetisation data for one specimen. Dolerite mean of 191°, -70°, α_{95}=18°, k=22.6, n=5.

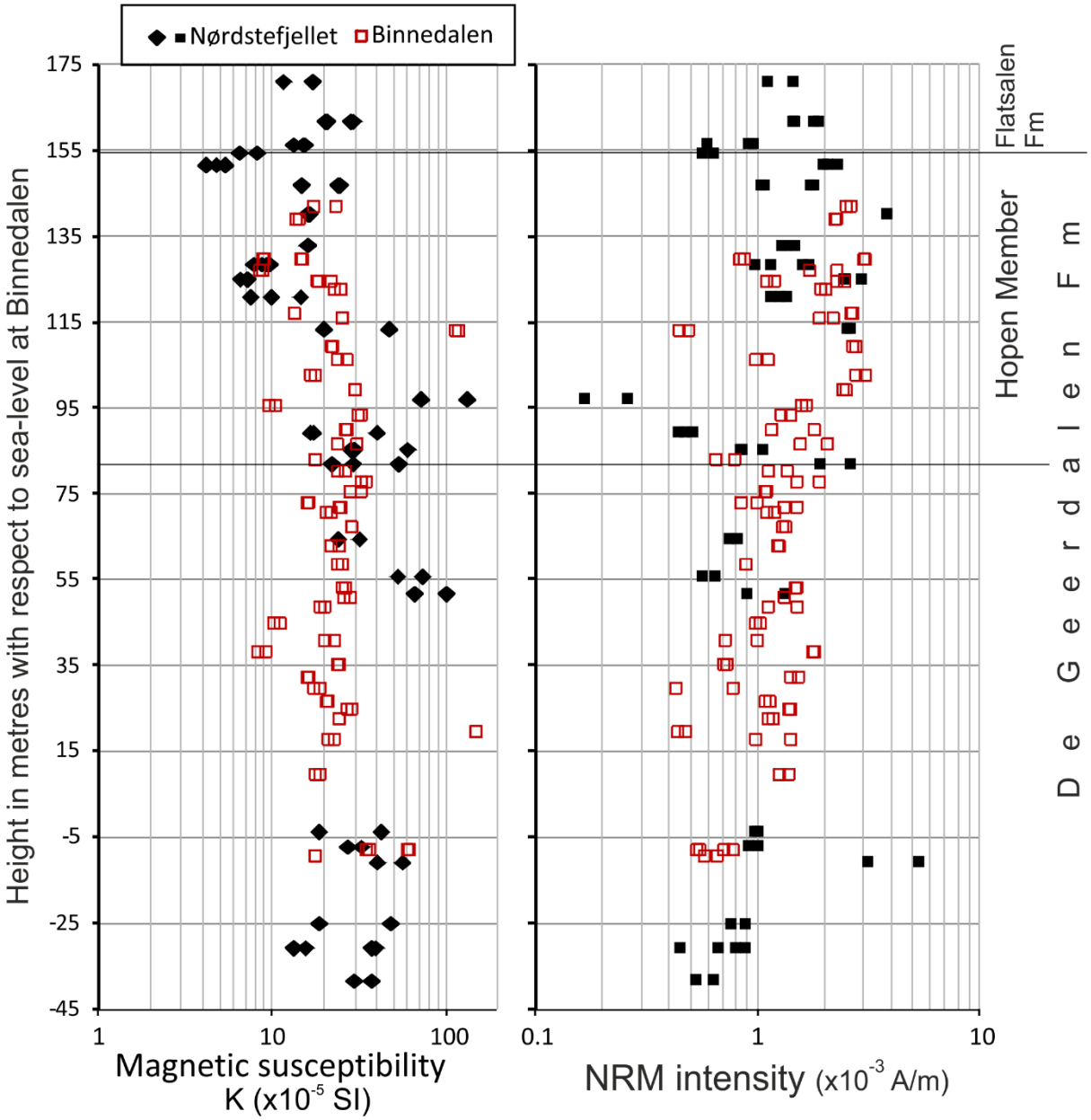

Fig. S4. Magnetic susceptibility (K) and NRM intensity for specimens from the Hopen sections. The NRM intensity values, show some stratigraphic variation, which may relate to Fe-oxide abundance differences between the Hopen Member and the other units.

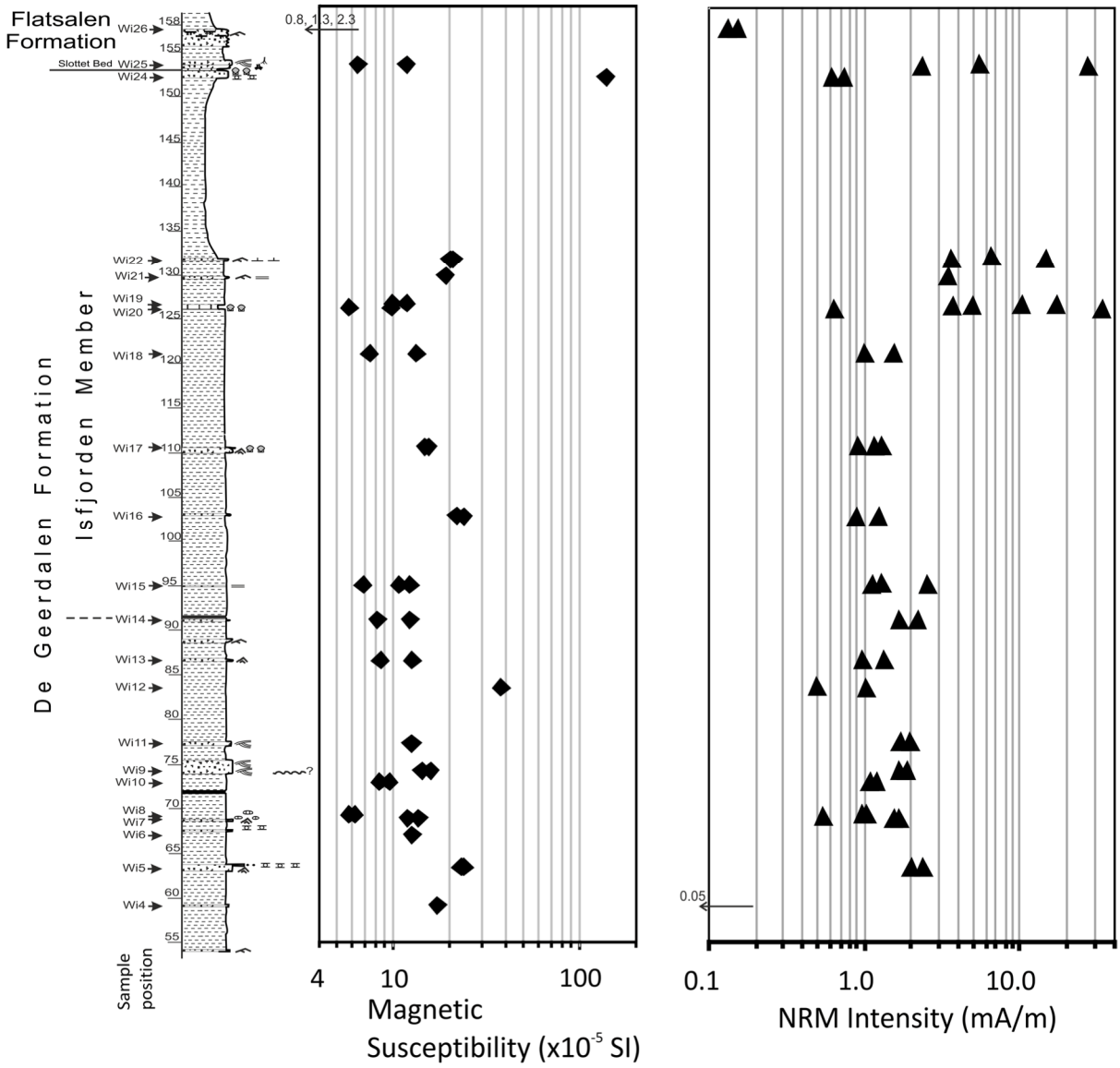

Fig. S5. Magnetic susceptibility and NRM intensity data of specimens from the Tumlingodden section.

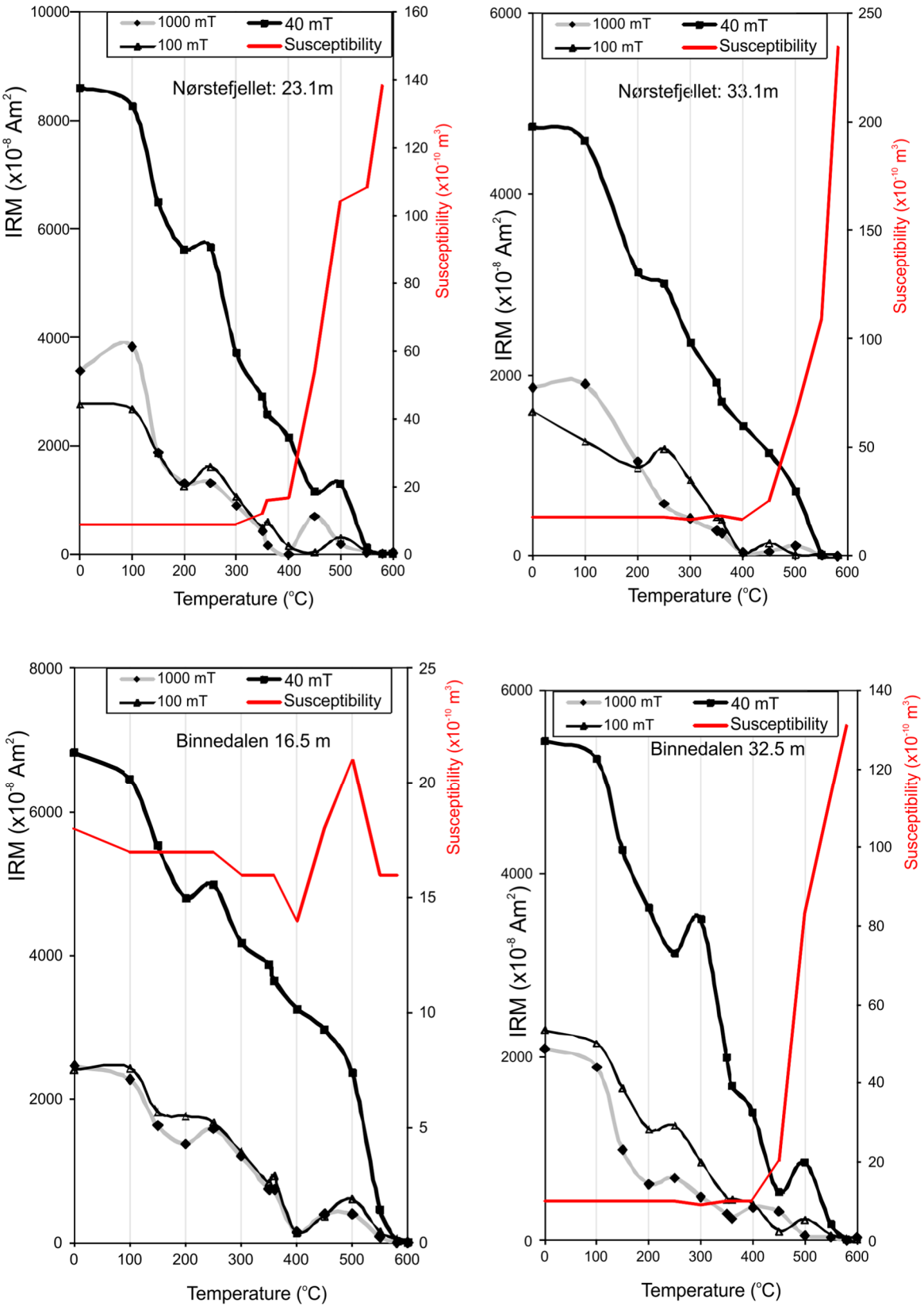

Fig. S6. Thermal demagnetisation of a 3-axis isothermal remanent magnetisation (IRM) with fields used at 40 mT, 100 mT and 1 T. The data here is rather noisy, in part due to the large thermal alteration at >300°C, but clearly shows the 40 mT coercivity fraction demagnetises at around 550°C, with the higher coercivity fractions between 400°C to 550°C. It is possible the consistent drop at 200°C may be a minispin calibration error for this step, rather than a real blocking temperature transition.

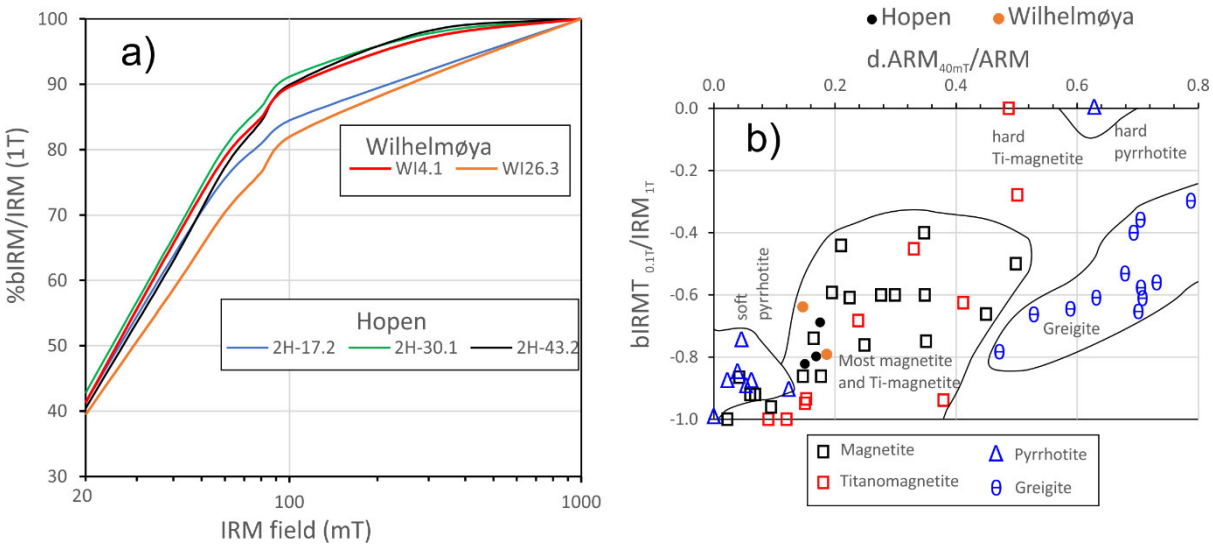

Fig. S7. Rock magnetic data from Binnedalen (Hopen) and Tumlingodden (Wilmhelmøya) sections. a) Isothermal remanent magnetisation (IRM) acquisition data, showing the near saturation at 300 mT, with most samples having a small high coercivity tail. The high coercivity tail is probably due to some haematite. Sample position WI4 andWI26 are shown in Fig. S5, and Binnedalen codes (2H-17,2H-30, 2h-43 are shown in main text Fig. 6. b) Data for these five samples plotted over the natural-mineral magnetic data of Peters & Thompson (1998), using the S-ratio ($bIRM_{0.1T}/IRM_{1T}$) and hardness of the anhysteretic remanence ($d.ARM_{40\,mT}$/ ARM which is: ARM tumble demagnetised at 40 mT field/ ARM acquired at 80mT AF, 0.1 mT DC bias field). This indicates that these samples have a very similar magnetic mineral content, falling over the soft end of the magnetite and titanomagnetite field. bIRM is the backfield magnetisation.

Specimen	χARM x10^{-8} m^3/Kg	d.ARM$_{40mT}$/ ARM	SIRM x10^{-5} Am^2/Kg	HIRM x10^{-5} Am^2/Kg	χARM/ SIRM x 10^{-3} mA^{-1}	Hcr (mT)	%HIRM	S-ratio (0.1T)	L-ratio
2H-17.2	41.1	0.18	50.6	4.00	0.81	27.8	7.9	-0.69	0.51
2H-30.1	40.8	0.15	46.6	1.05	0.88	26.1	2.3	-0.82	0.25
2H-43.2	27.8	0.17	43.4	0.80	0.64	28.5	1.8	-0.80	0.18
WI4.1	7.18	0.19	6.6	0.19	1.09	27.2	2.9	-0.79	0.28
WI26.3	5.43	0.15	12.0	1.05	0.45	31.0	8.8	-0.64	0.48

Table S1. Full set of mineral magnetic data for the specimens shown in Fig. S7. χARM= susceptibility of ARM, SIRM = IRM at 1T, HIRM= high field remanence between 0.3 and 1T. Hcr= coercivity of remanence (using DC backfield), %HIRM= percentage of the SIRM between 0.3- 1T. L-ratio is HIRM/[0.5*(SIRM+ $bIRM_{0.1T}$)] (Liu et al. 2007).

1. General magnetic properties of the samples

Magnetic susceptibility (K) and NRM intensity are strongly related to lithology and sediment body colour, with generally mudstones and claystones possessing the largest values of these parameters and well sorted sandstones generally the smallest (Fig. S8). There is evidence for the somewhat larger NRM intensity (i.e. those > 2 x10^{-3} A/m) of samples from the Hopen Member compared to units above and below this.

Broadly these magnetic data when combined with data from central Spitsbergen from the Botneheia, De Geerdalen and Tschermakfjellet formations define several groups of samples:

a) A cluster with low NRM intensities (<3 x10^{-3} A/m) and moderate K (12 to 50 x10^{-5} SI), which predominantly includes mudstone and sandstone samples from the De Geerdalen Fm, with some

samples from the Botneheia Fm (the *T-DG cluster*; Fig. S8);

b) A cluster with low K (<12 x10^{-5} SI), and low NRM intensity (<2 x10^{-3} A/m), marked as the *Botneheia cluster* in Fig. S8. This cluster predominantly represents samples from the Botneheia Fm mudstones, siltstones and shales (i.e. not concretions).

c) A group of siderite-bearing samples, with NRM intensity <3 x10^{-3} A/m but K >50 x10^{-5} SI*),* dominantly from the Tschermakfjellet Fm on Spitsbergen, but also some samples from Hopen (Fig. S8).

d) A group of samples with large NRM intensities (i.e. >2.5 x10^{-3} A/m), and K <20 x10^{-5} SI which includes samples from calcite concretions (‘*concretions cluster’*) from the Botneheia Fm (Fig. S8).

A number of competing factors related to magnetic-mineral abundance, and its mineralogy source probably account for these variations within the rocks.

1) In the grey-coloured lithologies the remanence carrying mineralogy is mostly in oxide form as magnetite (Fig. S7b), and contributes probably to the susceptibility but more importantly entirely to the remanence (i.e. NRM intensity). If the Fe-oxide content was entirely responsible for the magnetic susceptibility, there would normally be a positive relationship between NRM intensity and K values. This is not the case indicating there are other minerals responsible for the magnetic susceptibility variations in these units (Fig. S8).

2) Some types of Fe-bearing minerals such as chlorites, micas, siderite and ferroan dolomite can contribute to the magnetic susceptibility, but do not contribute to the NRM intensity. The few grey-coloured samples with K >50 x10^{-5} m^3, but NRM intensity < 3 x10^{-3} A/m are likely to be rich in siderite (Fig. S8).

3) The De Geerdalen Fm rocks show some stratigraphic separating in NRM intensity, with samples from the Hopen Member and the Isfjorden Member showing larger values compared to the mid-parts of the De Geerdalen Formation at Dalsnuten (Vendomdalen, Spitsbergen; Fig. S8). This may represent a provenance difference controlling the abundance of Fe-oxides in these sediments.

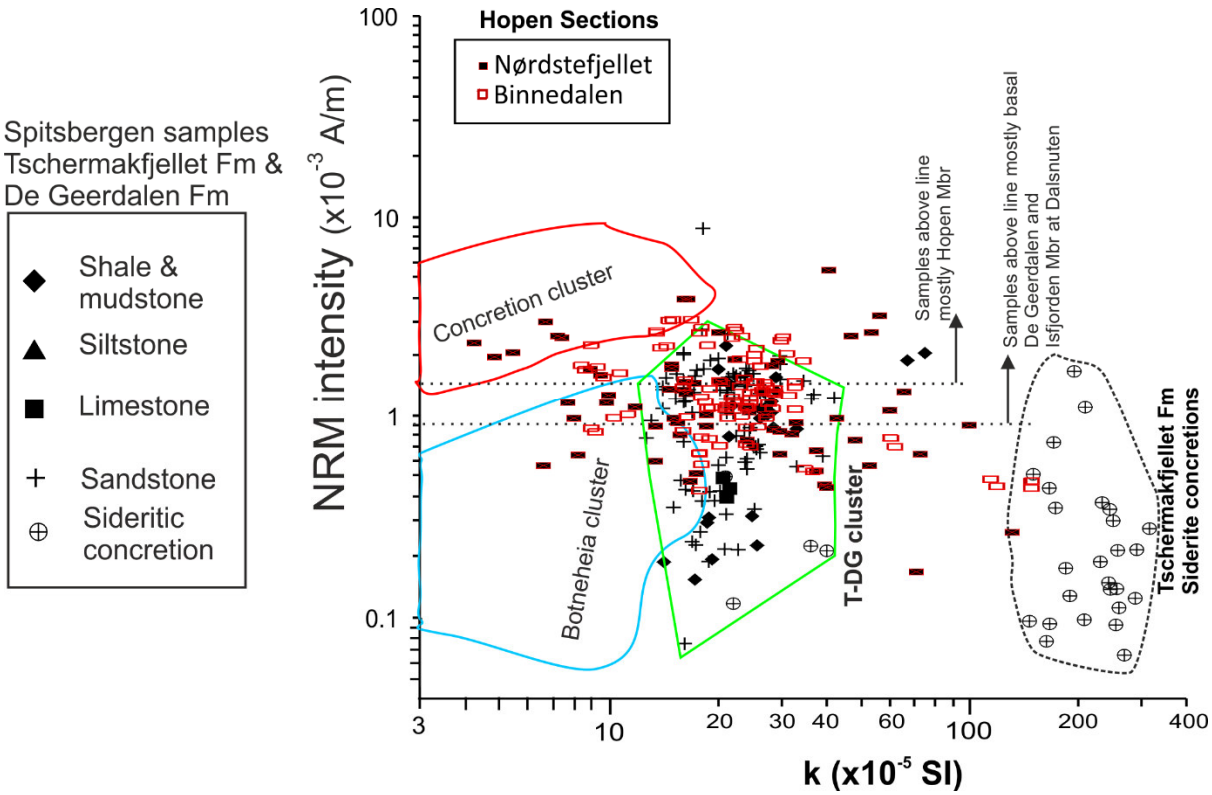

Fig.S8. Magnetic susceptibility (K) versus NRM intensity for specimens from Hopen and land based sections on Spitsbergen. Data from the Spitsbergen-sections of the Tschermakfjellet and De Geerdalen formations is indicated, and envelopes around 'Concretion' and 'Botheheia' data clusters are indicated. There is some evidence for stratigraphic separation of NRM intensity values, which may relate to provenance differences between the low, mid and upper parts of the De Geerdalen Fm. Land based data from Hounslow & Nawrocki (2008). Data points for the Botneheia and concretion clusters are not shown and are largely data from the Middle Triassic.

Section	Class	N	rho	α_{95} (°)	equivalent aMAD[1] (°)
Binnedalen	S1	5	1.8	5.2	0.9/1.1
	S2	21	1.4	9.1	1.5/2.0
[13, 87]	S3	14	2.1	15.4	2.6/3.3
	T1	10	2.1	15.9	2.7/3.4
	T2	21	2.0	17.3	2.9/3.7
[68,32]	T3	22	1.6	21.5	3.6/4.7
Nørstefjellet	S1	7	2.1	6.5	1.1/1.4
	S2	9	2.1	9.0	1.5/1.9
[30,70]	S3	4	2.1	8.8	1.5/1.9
	T1	7	2.2	21.3	3.6/4.6
	T2	14	2.3	17.0	2.8/3.7
[54,46]	T3	25	2.2	19.1	3.2/4.1
Tumlingodden	S1	2	1.7	10.5	1.8/2.3
	S2	0	-	-	-

[40,60]	S3	8	3.9	15.9	2.6/3.4
	T1	3	4.2	17.7	2.9/3.8
	T2	11	3.5	15.6	2.6/3.4
[64,36]	T3	16	2.9	21.5	3.6/4.6

Table S2. Statistics from the LINFIND fitting procedures applied to the demagnetisation classes. N= number in each category. Rho=median excess standard deviation, and α_{95} is mean of the 95% confidence interval as determined by LINEFIND (Kent et al., 1983). Details about using LINEFIND are in Hounslow et al. (2021). For T-class data this uncertainty is on the pole to the great circle. [1] two equivalent maximum angular deviation (MAD) angles are shown using Table 8 in Khoklov & Hulot (2016) with 3 and 5 points anchored- i.e. their C_{aMAD} (3) C_{aMAD} (5) conversion factors of 6.0, 4.63. For the better defined lines and planes with more data points aMAD will be an underestimate. Values in [..] are the number in S or T-class datasets with [origin, non-origin fits respectively].

Sample code	**%N_T (wt%)**	**%C (wt%)**	**$\delta^{13}C_{org}$ VPDB ($^0/_{00}$)**	**Height (m)**
Nørdstefjellet				
HO1	0.040	0.490	-25.21	-40.0
HO2	0.020	0.340	-28.95	-32.4
HO3	0.020	0.350	-28.76	-32.4
HO4	0.040	0.180	-24.66	-26.6
HO5	0.040	0.250	-24.97	-12.5
HO6	0.030	0.130	-24.53	-8.8
HO7	0.030	0.110	-24.20	-5.3
HO14	0.030	0.180	-24.36	44.3
HO15	0.050	0.240	-24.74	45.7
HO16	0.030	0.270	-24.08	54.5
HO18	0.010	0.070	-24.43	65.9
HO19	0.020	0.060	-25.94	71.1
HO20	0.010	0.040	-25.80	75.2
HO21	0.130	1.560	-24.74	81.8
HO22	0.050	1.030	-24.24	102.0
HO23	0.010	0.280	-28.14	111.4
HO24	0.020	0.260	-28.49	116.9
HO25	0.030	0.390	-28.34	122.0
HO26	0.030	0.260	-24.59	126.1
HO27	0.020	0.100	-26.07	134.5
HO28B	0.040	0.320	-25.19	141.5
HO29	0.006	0.020	-26.68	147.2

HO30	0.030	0.220	-26.90	149.7
HO31	0.030	0.400	-25.15	156.1
HO33	0.020	0.120	-26.68	170.8
Binnedalen				
1	0.020	0.060	-25.18	-10.7
2	0.070	0.880	-23.81	-9.3
3	0.010	0.360	-28.84	7.1
4	0.020	0.050	-25.35	9.7
5	0.040	0.180	-24.37	17.9
6	0.070	0.570	-24.39	19.8
7	0.040	0.200	-24.58	22.5
8	0.040	0.140	-24.92	24.9
9	0.050	0.090	-24.19	26.5
10	0.020	0.300	-29.20	29.7
11	0.030	0.270	-24.68	32.3
12	0.050	0.230	-24.52	35.3
13	0.020	0.090	-23.99	38.2
14	0.020	0.070	-24.62	40.7
15	0.010	0.050	-24.85	44.7
16	0.020	0.060	-25.86	48.7
17	0.080	1.100	-23.81	50.8
18	0.020	0.060	-25.41	53.1
19	0.030	0.050	-25.79	58.6
20	0.030	0.160	-24.48	62.9
21	0.040	0.190	-24.45	67.3
22	0.030	0.100	-24.00	69.8
23	0.030	0.160	-25.02	71.2
24	0.070	0.990	-24.32	72.5
25	0.010	0.040	-25.63	75.1
26	0.050	0.230	-24.52	77.5
27	0.040	0.250	-23.71	80.0
28	0.010	0.040	-25.18	83.0
29	0.090	1.260	-24.36	84.9
30	0.050	0.810	-24.92	87.7
31	0.070	0.990	-24.62	90.6

32	0.010	0.020	-25.77	92.4
33	0.060	0.850	-24.62	95.4
34	0.040	0.630	-24.26	98.3
35	0.050	0.900	-25.06	101.3
36	0.070	1.760	-24.43	104.1
37	0.120	1.740	-24.56	107.1
38	0.080	1.930	-23.97	108.5
39	0.040	0.610	-24.15	109.5
40	0.070	1.780	-24.31	110.4
41	0.100	1.500	-26.75	114.0
42	0.030	0.120	-27.16	114.9
43	0.020	0.130	-27.61	119.2
44	0.020	0.050	-25.24	122.2
45	0.040	0.200	-25.25	123.9
46	0.120	1.140	-24.32	126.2
47	0.030	0.090	-25.45	132.8
48	0.060	0.550	-24.07	137.3

Table S3. Organic carbon isotope data. Height is the composite height with respect to the log and section at Binnedalen. Values marked in red were not used, due to anomalous values. $\%N_T$, %C = total nitrogen and carbon.

Supplementary References

Hounslow, M.W. & Nawrocki, J. 2008: Palaeomagnetism and magnetostratigraphy of the Permian and Triassic of Spitsbergen: a review of progress and challenges. *Polar Research, 27*, 502-522.

Hounslow, M.W., Harris, S.E., Wójcik, K., Nawrocki, J., Ratcliffe,K., Woodcock, N.H. & Montgomery, P. 2021: A geomagnetic polarity stratigraphy for the Middle and Upper Ordovician. *Palaeogeography, Palaeoclimatology, Palaeoecology*, *567*, doi.org/10.1016/j.palaeo.2021.110225.

Johansen, S.K. 2016. *Sedimentology and facies distribution of the Upper Triassic De Geerdalen Formation in the Storfjorden area and Wilhelmøya, eastern Svalbard*. Msc thesis, NTNT Trondheim.

Kent, J.T., Briden, J.C. & Mardia, K.V. 1983: Linear and planar structure in ordered multivariate data as applied to progressive demagnetization of palaeomagnetic remanence. *Geophysical Journal International, 75*, 593-621.

Khokhlov, A. & Hulot, G. 2016: Principal component analysis of palaeomagnetic directions: converting a Maximum Angular Deviation (MAD) into a α_{95} angle. *Geophysical Journal International, 204*, 274–291.

Liu, Q., Roberts, A.P., Torrent, J., Horng, C.S. & Larrasoana, J.C. 2007: What do the HIRM and S-ratio really measure in environmental magnetism?. *Geochemistry, Geophysics, Geosystems, 8*, doi.org/10.1029/2007GC001717.